

Interface spaces based on physics for multiscale mixed methods applied to flows in fractured-like porous media

Franciane F. Rocha^a, Fabricio S. Sousa^{a,*}, Roberto F. Ausas^a, Felipe Pereira^b, Gustavo C. Buscaglia^a

^a*Instituto de Ciências Matemáticas e de Computação, Universidade de São Paulo, Av. Trabalhador São-carlense, 400, 13566-590, São Carlos, SP, Brazil*

^b*Department of Mathematical Sciences, The University of Texas at Dallas, 800 W. Campbell Road, Richardson, TX 75080-3021, USA*

Abstract

It is well known that domain-decomposition-based multiscale mixed methods rely on interface spaces, defined on the skeleton of the decomposition, to connect the solution among the non-overlapping subdomains. Usual spaces, such as polynomial-based ones, cannot properly represent high-contrast channelized features such as fractures (high permeability) and barriers (low permeability) for flows in heterogeneous porous media. We propose here new interface spaces, which are based on physics, to deal with permeability fields in the simultaneous presence of fractures and barriers, accommodated respectively, by the pressure and flux spaces. Existing multiscale methods based on mixed formulations can take advantage of the proposed interface spaces, however, in order to present and test our results, we use the newly developed Multiscale Robin Coupled Method (MRCM) [Guiraldello, et al., *J. Comput. Phys.*, 355 (2018) pp. 1-21], which generalizes most well-known multiscale mixed methods, and allows for the independent choice of the pressure and flux interface spaces. An adaptive version of the MRCM [Rocha, et al., *J. Comput. Phys.*, 409 (2020), 109316] is considered that automatically selects the physics-based pressure space for fractured structures and the physics-based flux space for regions with barriers, resulting in a procedure

*Corresponding author

Email addresses: `fr.franciane@usp.br` (Franciane F. Rocha), `fsimeoni@icmc.usp.br` (Fabricio S. Sousa), `rfausas@icmc.usp.br` (Roberto F. Ausas), `felipepereira62@gmail.com` (Felipe Pereira), `gustavo.buscaglia@icmc.usp.br` (Gustavo C. Buscaglia)

with unprecedented accuracy. The features of the proposed approach are investigated through several numerical simulations of single-phase and two-phase flows, in different heterogeneous porous media. The adaptive MRCM combined with the interface spaces based on physics provides promising results for challenging problems with the simultaneous presence of fractures and barriers.

Keywords: Multiscale Robin coupled method, multiscale mixed methods, interface spaces, two-phase flows, high-contrast porous media

1. Introduction

Simulations of petroleum reservoirs deal with highly heterogeneous permeability fields with multiple scales and high contrast. A representation of the solution that captures the heterogeneity requires several billion cells, making the numerical simulations extremely expensive [1]. The so-called *multiscale methods* have been introduced to exploit the multiscale structure of the problem and provide efficient approximations at a reduced computational cost [2]. The multiscale literature is vast and contemplates numerical implementations using techniques such as the finite volume method [3, 4], the primal finite element method [5, 6, 7], and several mixed finite element methods [8, 9, 10, 11, 12, 13].

The multiscale approaches solve the problem on a coarse decomposition of the domain, incorporating the fine-grid information through local basis functions. The accuracy of the multiscale methods is related to the calculation of the basis functions. If the heterogeneities are not well represented by the basis, inaccurate solutions are obtained. Spaces that are polynomial on the interfaces of the domain decomposition work well for smooth or Gaussian permeability fields, but their performance for high contrast, channelized ones is not satisfactory [14, 15, 16, 17]. To remedy this, informed spaces obtained from sets of snapshots by algebraic dimensionality reduction were considered in [7, 15, 17]. Another approach is to define the interface space through eigensolutions of local partial-differential problems [18]. These approaches can also be coupled to a-posteriori error estimators [14, 19, 20].

Other authors have looked for approaches more directly based on the geometry of the heterogeneities. In [21, 22, 23], for example, the authors consider polynomial bases but adapt the grid to the geological properties, while in [24, 16, 25] local enrichment functions were added on high-permeability

regions. These geometrical strategies are well suited for permeability fields containing either channels or barriers, but not both. In this contribution, we propose a strategy to deal with the simultaneous presence of channels and barriers, since such situation is not unfrequent in reservoir simulation [26]. For this purpose, we take advantage of the Multiscale Robin Coupled Method (MRCM, [27]), which allows for the independent choice of the pressure and flux interface spaces. In fact, the pressure space is designed so as to accommodate channels and the flux space to accommodate barriers, and the adaptive version of the MRCM [28] is used to automatically select the appropriate parameters at each location.

Our intention is to use high-definition volumetric grids that capture the large scale features of the fracture network, especially when they are relatively large as happens in fractured karst reservoirs [29, 30, 31, 32]. Typically, fractures are handled with separate discrete models that represent the fractures as lower-dimensional objects so as to incorporate sub-grid resolution [33, 34, 35, 36, 37, 38]. A popular approach is the Discrete Fracture Model (DFM) which uses unstructured grids to place fractures at the interface between matrix cells [39, 40, 41]. Other approaches are the Embedded DFM [42, 43], the multi-continuum model [44, 45] and the hierarchical fracture models [46, 47, 48].

Since it is possible to combine discrete models with multiscale methods [49, 50, 51, 52], the final goal of the improved MRCM proposed here is to allow a unified treatment of fractured karst reservoirs in which the modeling of the fractures is shared, depending on the fracture’s size, between the volumetric grid and the discrete models. For this reason, we consider here permeability fields containing multiple narrow and relatively straight features (channels, barriers) that mimic the largest structures of a fractured porous medium, and refer to them as “fractured-like” fields. The accuracy and efficiency of the proposed method are investigated through several numerical simulations of fractured-like reservoirs both in single-phase and two-phase (oil-water) situations.

The paper is organized as follows. In Section 2 we introduce the model problem and numerical approximation. The MRCM is briefly recalled in Section 3 followed by Section 4, where the strategies for building the physics-based interface spaces are presented along with some numerical experiments. In section 5 we explain our proposed combination of the physics-based spaces with the adaptive MRCM. Numerical experiments for single and two-phase flows are presented in Section 6. Finally, the paper is concluded in Section

7.

2. Model problem

We consider a high-contrast heterogeneous oil reservoir through which an immiscible and incompressible single-phase or multiphase flow takes place. The heterogeneity of the medium is represented by a space-dependent permeability coefficient in the elliptic Darcy model. This coefficient exhibits variations of many orders of magnitude over short distances. For simplicity, the capillary pressure and gravity effects are not considered.

2.1. Single-phase model

The unknowns considered in the single-phase model are the Darcy velocity $\mathbf{u}(\mathbf{x}, t)$ and the fluid pressure $p(\mathbf{x}, t)$. The governing equations are the Darcy's law with a statement of conservation of mass, given by

$$\begin{aligned} \mathbf{u} &= -K(\mathbf{x})\nabla p && \text{in } \Omega \\ \nabla \cdot \mathbf{u} &= q && \text{in } \Omega \\ p &= g && \text{on } \partial\Omega_p \\ \mathbf{u} \cdot \mathbf{n} &= z && \text{on } \partial\Omega_u \end{aligned} \tag{1}$$

where $\Omega \subset \mathbb{R}^2$ is the computational domain; $K(\mathbf{x})$ is the symmetric, uniformly positive definite absolute permeability tensor; $q = q(\mathbf{x}, t)$ is a source term; $g = g(\mathbf{x}, t)$ is the pressure condition specified at the boundary $\partial\Omega_p$ and $z = z(\mathbf{x}, t)$ is the normal velocity condition (\mathbf{n} is the outward unit normal) specified at the boundary $\partial\Omega_u$.

2.2. Two-phase model

In the context of two-phase flows of water and oil (denoted by w and o , respectively), we consider that the reservoir contains injection wells, from which water is injected to displace the trapped oil towards production wells. The oil and water saturations are the new unknowns. These saturations are related considering a fully saturated medium (the sum of both oil and water saturation is equal to one). Therefore the model considers only the water saturation $s(\mathbf{x}, t)$ in the transport problem. Here the elliptic problem (1) is written as

$$\begin{aligned} \mathbf{u} &= -\lambda(s)K(\mathbf{x})\nabla p && \text{in } \Omega \\ \nabla \cdot \mathbf{u} &= q && \text{in } \Omega \\ p &= g && \text{on } \partial\Omega_p \\ \mathbf{u} \cdot \mathbf{n} &= z && \text{on } \partial\Omega_u \end{aligned} \tag{2}$$

and coupled with the hyperbolic conservation law for the transport of water saturation [53, 54], which is given by

$$\begin{aligned} \frac{\partial s}{\partial t} + \nabla \cdot (f(s)\mathbf{u}) &= 0 && \text{in } \Omega \\ s(\mathbf{x}, t = 0) &= s^0(\mathbf{x}) && \text{in } \Omega \\ s(\mathbf{x}, t) &= \bar{s}(\mathbf{x}, t) && \text{in } \partial\Omega^- \end{aligned} \quad (3)$$

where s^0 is the initial condition for the saturation and \bar{s} is the saturation at the inlet boundaries $\partial\Omega^- = \{\mathbf{x} \in \partial\Omega, \mathbf{u} \cdot \mathbf{n} < 0\}$. The total mobility $\lambda(s) = \lambda_w(s) + \lambda_o(s)$ and the fractional flow of water $f(s)$ are respectively given by

$$\lambda(s) = \frac{k_{rw}(s)}{\mu_w} + \frac{k_{ro}(s)}{\mu_o} \quad \text{and} \quad f(s) = \frac{\lambda_w(s)}{\lambda(s)}, \quad (4)$$

where $k_{rj}(s)$ and μ_j , $j \in \{w, o\}$, are respectively the relative permeability function and viscosity of phase j . For simplicity, the porosity is considered constant both in space and time and consequently, it can be easily scaled out by changing the time variable.

2.3. Numerical approximation

For computing single phase flows we solve directly the elliptic problem (1) by the Multiscale Robin Coupled Method (MRCM). To simulate two-phase flows we solve the system (2)-(3) using an operator splitting procedure, in which we solve (2) to compute $p(\mathbf{x}, t)$ and $\mathbf{u}(\mathbf{x}, t)$ and (3) for $s(\mathbf{x}, t)$, sequentially [55]. We use the MRCM to solve the elliptic problem (2), and the upwind method [56] for the transport of saturation (3), in which a CFL-type condition is enforced. The splitting procedure considers larger time steps for the elliptic problem compared to those used for the hyperbolic equation ([55]) improving the computational efficiency.

We consider the relation $\Delta t_p = C\Delta t_s$, where Δt_s is the time step for the saturation equation (for simplicity assumed constant but in practice we allow for variable Δt_s), Δt_p is the time step for the elliptic problem and C is a positive integer. The elliptic problem is solved at times $t_n = n\Delta t_p$, for $n = 0, 1, \dots$, where we compute $p^n(\mathbf{x})$ and $\mathbf{u}^n(\mathbf{x})$ using the water saturation $s^n(\mathbf{x})$ at time $t = t_n$. The saturation equation is solved at intermediate times $t_{n,k} = t_n + k\Delta t_s$, for $k = 1, 2, \dots, C$, such that $t_n < t_{n,k} \leq t_{n+1}$. For each

saturation time step $t = t_{n,k}$ we set the velocity $\mathbf{u}^{n,k}$ to the following linear extrapolated value

$$\mathbf{u}^{n,k}(\mathbf{x}, t) = \begin{cases} \mathbf{u}^0(\mathbf{x}), & \text{if } 0 \leq t \leq t_1, \\ \frac{t - t_{n-1}}{\Delta t_p} \mathbf{u}^n(\mathbf{x}) - \frac{t - t_n}{\Delta t_p} \mathbf{u}^{n-1}(\mathbf{x}), & \text{if } t_n < t \leq t_{n+1}, \end{cases} \quad (5)$$

where $\mathbf{u}^n(\mathbf{x})$ is the velocity obtained from Equation (2) at time $t = t_n$, approximating $\mathbf{u}(\mathbf{x}, t_n)$ (see [55]).

3. The multiscale Robin coupled method

In this paper, we use the MRCM to approximate the Equation (1) for single-phase flows and the Equation (2) for two-phase flows. For simplicity, we drop the time dependency and obtain the following elliptic problem

$$\begin{aligned} \mathbf{u} &= -\kappa(\mathbf{x})\nabla p && \text{in } \Omega \\ \nabla \cdot \mathbf{u} &= q && \text{in } \Omega \\ p &= g && \text{on } \partial\Omega_p \\ \mathbf{u} \cdot \mathbf{n} &= z && \text{on } \partial\Omega_u \end{aligned} \quad (6)$$

where $\kappa = K(\mathbf{x})$ for single-phase and $\kappa = \lambda(s(\mathbf{x}))K(\mathbf{x})$ for two-phase flows.

The MRCM considers a decomposition of the domain Ω into non-overlapping subdomains Ω_i , $i = 1, 2, \dots, N$. Continuity of the normal fluxes and pressure are weakly imposed on a coarse scale H , which is significantly larger than the fine-scale of the discretization h . Here H is the characteristic size of the subdomains. The weak continuities are enforced to the multiscale solution (\mathbf{u}_h, p_h) at the skeleton Γ of the decomposition (union of all interfaces $\Gamma_{ij} = \Omega_i \cap \Omega_j$) by the following compatibility conditions

$$\int_{\Gamma} (\mathbf{u}_h^+ - \mathbf{u}_h^-) \cdot \check{\mathbf{n}} \psi \, d\Gamma = 0 \quad \text{and} \quad \int_{\Gamma} (p_h^+ - p_h^-) \phi \, d\Gamma = 0 \quad (7)$$

for all $(\phi, \psi) \in \mathcal{U}_H \times \mathcal{P}_H$, which are the interface spaces defined over the edges \mathcal{E}_h of the skeleton Γ . Here $\check{\mathbf{n}}$ is a fixed normal vector to the skeleton Γ , pointing outwards from the subdomain with the smallest index. The solution on each side of the interface Γ is represented by the + and - superscripts. The solution inside each subdomain (\mathbf{u}_h^i, p_h^i) is related to the normal flux

and pressure unknowns at the interfaces $(U_H, P_H) \in \mathcal{U}_H \times \mathcal{P}_H$ by the Robin boundary conditions on the local problems

$$-\frac{\alpha(\mathbf{x})H}{\kappa_i(\mathbf{x})} \mathbf{u}_h^i \cdot \check{\mathbf{n}}^i + p_h^i = -\frac{\alpha(\mathbf{x})H}{\kappa_i(\mathbf{x})} U_H \check{\mathbf{n}} \cdot \check{\mathbf{n}}^i + P_H, \quad \mathbf{x} \in \Gamma_{i,j}, \quad (8)$$

where the $\check{\mathbf{n}}^i$ is the normal vector to Γ pointing outwards of Ω_i . The parameter for the Robin boundary condition in Equation (8) is given by

$$\beta_i(\mathbf{x}) = \frac{\alpha(\mathbf{x})H}{\kappa_i(\mathbf{x})}, \quad (9)$$

where $\alpha(\mathbf{x})$ is a dimensionless algorithmic function that takes different values according to the permeability field (in the context of the adaptive MRCM). We remark that by changing α we recover the Multiscale Mortar Mixed Finite Element Method (MMMFEM, [10]) when $\alpha \rightarrow 0$ and the Multiscale Hybrid-Mixed Finite Element Method (MHM, [11]) when $\alpha \rightarrow +\infty$. The solution given by the Multiscale Mixed Method (MuMM, [12]) can also be recovered under the right choice of parameters. The interested reader is referred to [27] for more details.

The differential formulation of the MRCM consists in finding local solutions (\mathbf{u}_h^i, p_h^i) into each subdomain Ω_i , and global interface unknowns (U_H, P_H) satisfying the local problems

$$\begin{aligned} \mathbf{u}_h^i &= -\kappa(\mathbf{x}) \nabla p_h^i && \text{in } \Omega_i \\ \nabla \cdot \mathbf{u}_h^i &= q && \text{in } \Omega_i \\ p_h^i &= g && \text{on } \partial\Omega_i \cap \partial\Omega_p \\ \mathbf{u}_h^i \cdot \check{\mathbf{n}}^i &= z && \text{on } \partial\Omega_i \cap \partial\Omega_u \\ -\beta_i \mathbf{u}_h^i \cdot \check{\mathbf{n}}^i + p_h^i &= -\beta_i U_H \check{\mathbf{n}} \cdot \check{\mathbf{n}}^i + P_H && \text{on } \partial\Omega_i \cap \Gamma \end{aligned} \quad (10)$$

and the compatibility conditions

$$\begin{aligned} \sum_{i=1}^N \int_{\partial\Omega_i \cap \Gamma} (\mathbf{u}_h^i \cdot \check{\mathbf{n}}^i) \psi \, d\Gamma &= 0 \\ \sum_{i=1}^N \int_{\partial\Omega_i \cap \Gamma} \beta_i (\mathbf{u}_h^i \cdot \check{\mathbf{n}}^i - U_H \check{\mathbf{n}} \cdot \check{\mathbf{n}}^i) \phi (\check{\mathbf{n}} \cdot \check{\mathbf{n}}^i) \, d\Gamma &= 0 \end{aligned} \quad (11)$$

for all $(\phi, \psi) \in \mathcal{U}_H \times \mathcal{P}_H$.

The interface spaces \mathcal{U}_H and \mathcal{P}_H are defined over the skeleton Γ as subspaces of

$$F_h(\mathcal{E}_h) = \{f : \mathcal{E}_h \rightarrow \mathbb{R}; f|_e \in \mathbb{P}_0, \forall e \in \mathcal{E}_h\}, \quad (12)$$

where \mathcal{E}_h is the set of all edges of the skeleton Γ [27]. These spaces are local and independently built on each interface $\Gamma_{i,j}$ and spanned by the multiscale basis functions $\{\phi_1, \phi_2, \dots, \phi_{N_U}\}$ and $\{\psi_1, \psi_2, \dots, \psi_{N_P}\}$, where N_U and N_P are the respective dimensions of the interface spaces (see [27] for more details). The multiscale basis functions are obtained by solving the local problems in Equations (10), that can be computed in parallel. These basis functions are further used to compute the global solution as a linear combination, whose coefficients are obtained by the solution of the global interface system generated by Equations (11).

In the previous works, the authors consider the interface spaces \mathcal{U}_H and \mathcal{P}_H as low-dimensional polynomial spaces [27] or informed spaces [17] for the MRCM. In the next section, we propose alternative physics-based interface spaces to improve the accuracy of the multiscale solution of the elliptic problem. These interface spaces are built to capture variations of the permeability field, especially those characterized by fractures and barriers.

4. Physics-based interface spaces

Low-dimensional polynomial spaces are not robust to represent variations of high-contrast permeability fields containing channelized structures as fractures and barriers. Even informed spaces with a low number of degrees of freedom are not enough. To better represent the variations of fractured-like permeability fields we present two physics-based interface spaces. The idea is to build the multiscale basis functions based on the pressure and flux solutions at each channelized structure (fracture/barrier). We present one space for pressure and another for flux. The new pressure space is suited for high permeability channels, whereas the new flux space for barriers or low permeability barriers, that cross the interface between subdomains.

The support of the new basis functions are the interfaces that contain channelized structures. In the remaining interfaces the spaces can be freely chosen (any low-dimensional polynomial or informed spaces). We denote $(\mathcal{U}_{H,k}, \mathcal{P}_{H,k})$ the choice of the interface spaces made up of the elementwise constant fine grid representation of polynomials over the interface elements, where k is the degree of the polynomial. To introduce the concept we consider, for simplicity, the linear spaces $(\mathcal{U}_{H,1}, \mathcal{P}_{H,1})$ for both pressure and flux.

This choice of interface spaces is used further in the numerical section. The basis of these spaces contain $N_P = 2$ and $N_U = 2$ functions on each interface between two subdomains. If the permeability field contains fractures passing through the interface we propose to replace the space $\mathcal{P}_{H,1}$ by the physics-based pressure space. On the other hand, if the permeability field contains barriers crossing the interface we replace the space $\mathcal{U}_{H,1}$ by the physics-based flux space. In the following subsections, we describe how the physics-based interface spaces are built for capturing the high-contrast structures.

4.1. A physics-based interface space for the pressure

We define a simplified problem test to show the behavior of the solution to define the interface spaces. In Figure 1 we consider a high-contrast permeability field containing a vertical fracture Figure 1(a). We show the pressure Figure 1(b) and flux Figure 1(c) fine grid solutions. The flow is established by imposing a flux boundary condition from left to right and no-flow at top and bottom. This geometry induces a one-dimensional pressure solution which is plotted along a horizontal line in Figure 1(d). Notice, the pressure is essentially constant over the fracture region. Any domain decomposition with more than one subdomain in the y -direction contains horizontal interfaces through which the fracture passes. Let Γ^{frac} be the set of all interfaces that contain at least one fine cell in which the absolute permeability is larger than a cutoff value ζ_{max} . We intend to replace the pressure linear space $\mathcal{P}_{H,1} = \text{span}\{\psi_1, \psi_2\}$ at the interfaces $\Gamma_{i,j} \subset \Gamma^{\text{frac}}$ by a physics-based pressure space, denoted by \mathcal{P}_H^* .

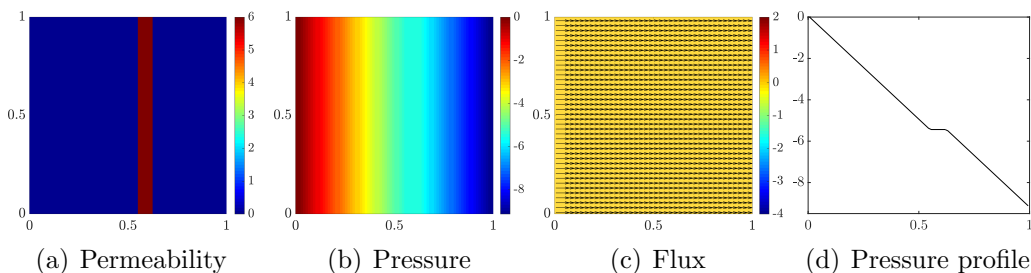


Figure 1: Vertical fracture problem. (a) Permeability field (log-scaled) containing a vertical fracture. (b) Pressure field. (c) Flux. The colors in the flux plot refer to the log-scale flux magnitude. (d) Pressure along a horizontal line.

The new pressure space mimics the behavior of the pressure across the

fractures. Let $\Gamma_{i,j} \subset \Gamma^{\text{frac}}$ be an interface with support in $[a, d]$ through which a fracture passes in $[b, c] \subset [a, d]$, as sketched in Figure 2. The basis functions are defined as:

$$\psi_1^*(x) = \begin{cases} \frac{b-x}{b-a} & \text{if } x \in (a, b) \\ 0 & \text{otherwise} \end{cases} \quad (13)$$

$$\psi_2^*(x) = \begin{cases} \frac{x-a}{b-a} & \text{if } x \in (a, b) \\ 1 & \text{if } x \in (b, c) \\ \frac{d-x}{d-c} & \text{if } x \in (c, d) \end{cases} \quad (14)$$

$$\psi_3^*(x) = \begin{cases} \frac{x-c}{d-c} & \text{if } x \in (c, d) \\ 0 & \text{otherwise} \end{cases} \quad (15)$$

The new interface pressure space is then defined as $\mathcal{P}_H^* = \text{span}\{\psi_1^*, \psi_2^*, \psi_3^*\}$ at $\Gamma_{i,j} \subset \Gamma^{\text{frac}}$. Since the definition of the basis depends only on the fine-grid discretization of the permeability at the interface, any fracture crossing the interface can be represented. Therefore, these basis functions are not restricted to fractures orthogonal to the interface. If the interface contains more than one fracture we need to define a new basis function with similar behavior to the ψ_2^* for each fracture. The total number of basis functions per interface is thus $2 + N_{\text{frac}}$, where N_{frac} is the number of fractures at the interface.

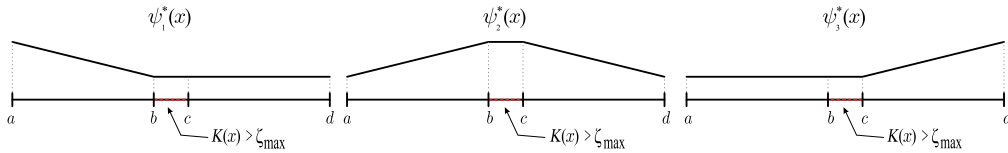


Figure 2: Physics-based basis functions for pressure at the interfaces that contain fractures. Note that the set of functions is able to capture the pressure profile across the fracture.

In Figure 3, we show the pressure solution at the horizontal line $y = 0.49$ delivered by the MMMFEM (by setting the α parameter of the MRCM to the value 10^{-6}) in a domain decomposition with 2×2 coarse cells. We denote by MMMFEM-PBS the multiscale method combined with the physics-based

spaces and by MMMFEM-POL the multiscale method combined with polynomial spaces (linear in this paper). We note that for both single (Figure 3(a) and Figure 3(c)) and multiple (Figure 3(b) and Figure 3(d)) fractures the correct pressure solution is only captured by the MMMFEM combined with physics-based interface spaces.

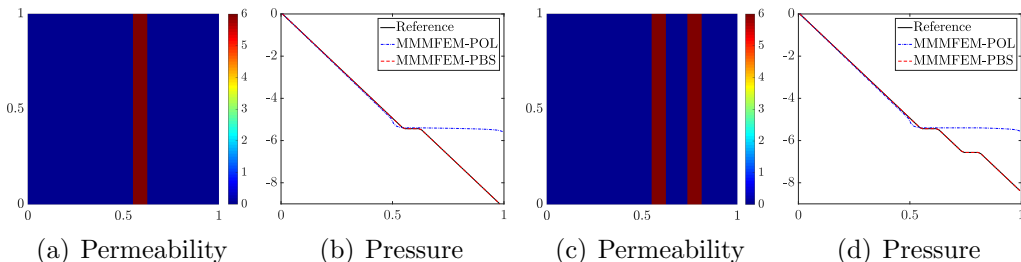


Figure 3: High-contrast permeability field (log-scaled) with one (a) and two fractures (c). Pressure solutions for one (b) and two fractures (d) computed by the fine-grid solver and the multiscale ones MMMFEM-POL and MMMFEM-PBS. We note that for both one and two fractures the correct pressure solution is only captured by the MMMFEM-PBS.

4.2. A physics-based interface space for the flux

Now we focus on fields containing barriers. Once again we define a simplified problem to motivate the interface spaces. In Figure 4(a) we consider a high-contrast permeability field containing a horizontal barrier. We show the fine grid solutions for pressure Figure 4(b) and for flux Figure 4(c). Here the flow is established by imposing a pressure gradient from left to right and no-flow at top and bottom. The x -component of the flux along a vertical line is illustrated in Figure 4(d), showing the discontinuities at the locations of transitions to barrier regions. Any domain decomposition with more than one subdomain in x -direction contains vertical interfaces through which the barrier passes. Let Γ^{barrier} be the set of all the interfaces that contain at least one fine cell in which the absolute permeability is lower than a cutoff value ζ_{\min} . We introduce the new flux spaces \mathcal{U}_H^* according to the behavior of the flux solution by replacing the flux linear spaces $\mathcal{U}_{H,1} = \text{span}\{\phi_1, \phi_2\}$ at the interfaces $\Gamma_{i,j} \subset \Gamma^{\text{barrier}}$.

Let $\Gamma_{i,j} \subset \Gamma^{\text{barrier}}$ be an interface with support in $[a, d]$ through which a barrier passes in $[b, c] \subset [a, d]$, as sketched in Figure 5. We define the

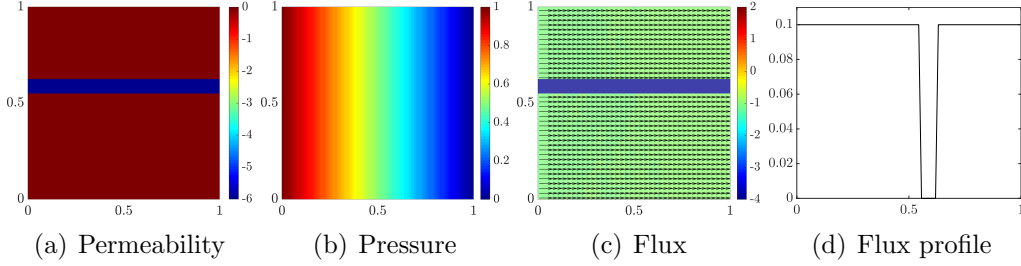


Figure 4: Horizontal barrier problem. (a) Permeability field (log-scaled) containing a horizontal barrier. (b) Pressure field. (c) Flux. The colors in the flux plot refer to the log-scale flux magnitude. Additionally, the x -component solution of the flux along a vertical line is illustrated in (d), where we note that the flux is discontinuous at the transitions to barrier regions.

following basis functions:

$$\phi_1^*(x) = \begin{cases} 1 & \text{if } x \in (a, b) \\ 0 & \text{otherwise} \end{cases} \quad (16)$$

$$\phi_2^*(x) = \begin{cases} 1 & \text{if } x \in (b, c) \\ 0 & \text{otherwise} \end{cases} \quad (17)$$

$$\phi_3^*(x) = \begin{cases} 1 & \text{if } x \in (c, d) \\ 0 & \text{otherwise} \end{cases} \quad (18)$$

The new interface space is defined as $\mathcal{U}_H^* = \text{span}\{\phi_1^*, \phi_2^*, \phi_3^*\}$ at $\Gamma_{i,j}^{\text{barrier}}$. These basis functions are not restricted to barriers orthogonal to the interface, similar to the pressure basis. If the interface contains more than one barrier we need to define a new basis function with behavior similar to that of the ϕ_2^* for each barrier, plus a constant function for each region between two barriers. The total number of basis functions per interface is thus $1 + 2N_{\text{barrier}}$, where N_{barrier} is the number of barriers.

In Figure 6 we show the x -component of the flux along $x = 0.5$ provided by the MHM (by setting the α parameter of the MRCM to the value 10^6) in a domain decomposition with 2×2 coarse cells. We compare the approximations provided by the MHM-POL (MHM combined with the linear spaces) and MHM-PBS (MHM combined with the physics-based spaces) with the fine-grid solution. We note that for both single (Figure 6(a) and Figure 6(c)) and multiple (Figure 6(b) and Figure 6(d)) barriers the correct x -component of the flux is only captured by MHM-PBS.

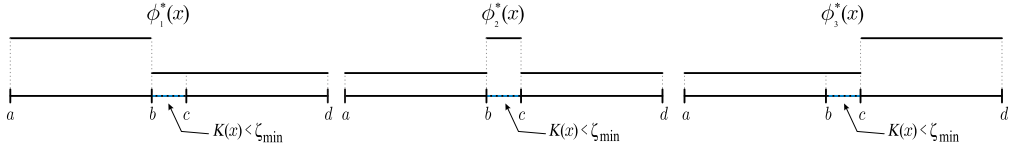


Figure 5: Physics-based basis functions for flux at the interfaces that contain barriers.

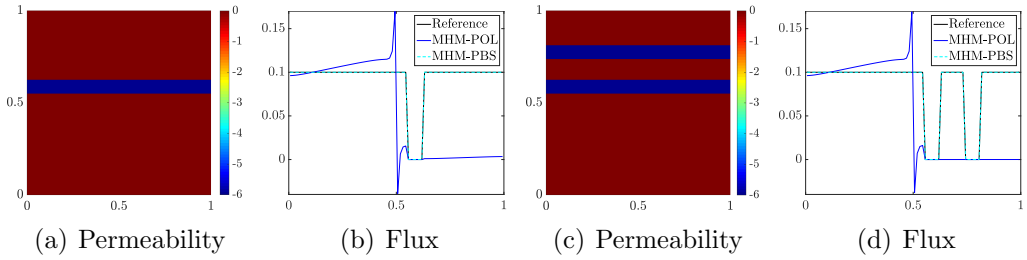


Figure 6: High-contrast permeability field (log-scaled) with one (a) and two barriers (c). Fine-grid reference, MHM-POL and MHM-PBS solutions for the x -component of the flux considering one (c) and two barriers (d). Notice that for both one and two barriers the correct x -flux solution is only captured by the MHM-PBS.

4.3. Experiments with the physics-based interface spaces

The examples in Figure 3 and Figure 6 illustrate that the usual linear interface spaces fail to approximate the solution in the presence of fractures and barriers even for simple problems. The proposed physics-based spaces have been able to represent the behavior of the solution in those problems. In this subsection, we show that the physics-based spaces work well also in slightly more complex permeability fields. Initially, we consider a permeability field with fractures and use the physics-based pressure space combined with the MMMFEM. Then we consider a permeability field with barriers and use the physics-based flux space combined with the MHM.

4.3.1. The MMMFEM for permeability fields with fractures

The first study considers a permeability field containing fractures. In this case, the physics-based pressure space is applied to the interfaces that contain cells in which the absolute permeability is larger than a cutoff value ζ_{\max} . We combine the new interface space with the MMMFEM. We consider the permeability in the fracture, K_{\max} varying from 10 to 10^8 whereas the background is homogeneous with $K = 1$, see Figure 7 (a). The cutoff value set to capture the fractures is $\zeta_{\max} = 1$ in all cases. The domain considered is $\Omega = [0, 1] \times [0, 1]$ containing 160×160 cells. In Figure 7 (b) we show the relative $L^2(\Omega)$ errors for pressure as function of the permeability contrast. Three domain decompositions are considered: 4×4 , 8×8 and 16×16 coarse cells, each one containing, respectively 40×40 , 20×20 and 10×10 fine cells. The boundary conditions in the simulations of this subsection are no-flow at the top and bottom boundaries along with an imposed flux on the left and right boundaries. No source terms are considered. We compare the multiscale solution considering the usual linear polynomial (MMMFEM-POL) and the physics-based (MMMFEM-PBS) pressure interface spaces. We note that for permeability contrasts larger than 100 the improvement with the physics-based spaces is significant for all the domain decompositions considered. Domain decompositions with more subdomains present smaller errors. Figure 8 shows the pressure approximations for the decomposition of 8×8 coarse cells in the highest permeability contrast $K_{\max}/K_{\min} = 10^8$. It is clear that the imprecisions of the MMMFEM solution with the linear interface spaces are corrected with the use of the physics-based ones.

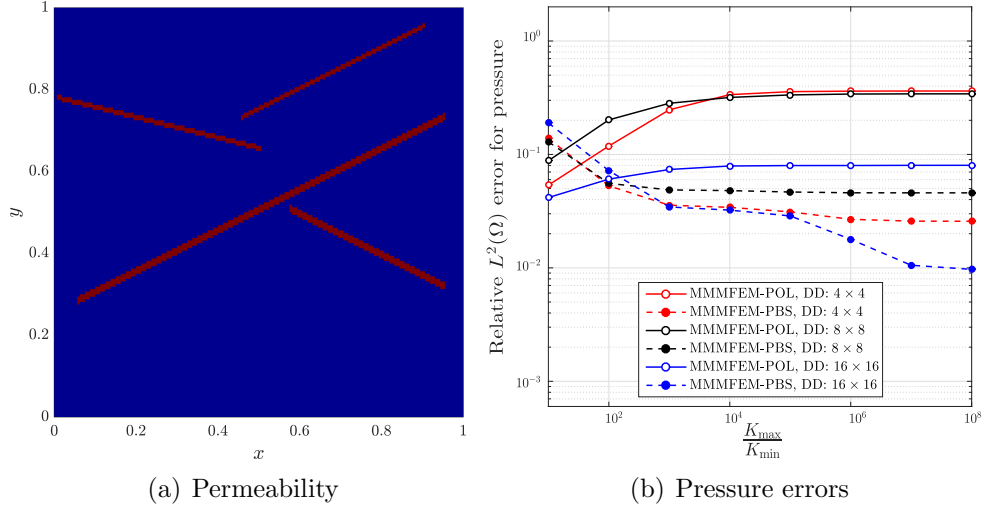


Figure 7: High-contrast permeability field with fractures (a). We consider the permeability in the fracture, K_{\max} varying from 10 to 10^8 whereas the background is homogeneous with $K = 1$. Relative $L^2(\Omega)$ pressure errors as function of the contrast are shown for the MMMFEM-POL and MMMFEM-PBS (b). Three domain decompositions are considered: with 4×4 , 8×8 and 16×16 coarse cells. We note a significant improvement for the MMMFEM-PBS in all the meshes, especially for high-contrast.

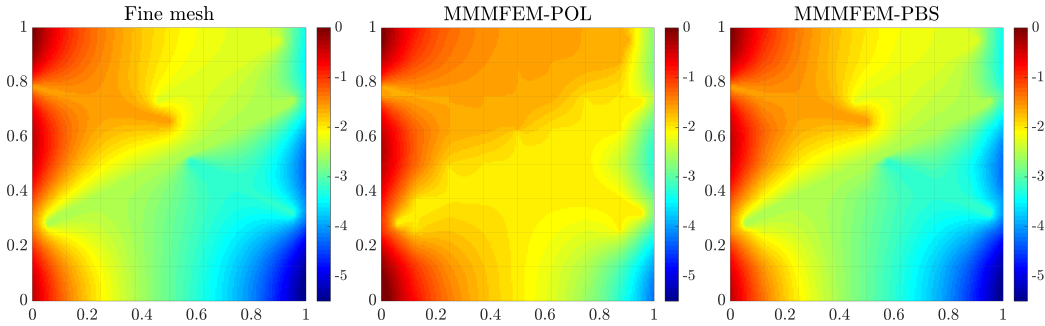


Figure 8: Pressure approximations considering the contrast of $K_{\max}/K_{\min} = 10^8$. Left to right: fine mesh, MMMFEM-POL, and MMMFEM-PBS solutions. The domain decomposition considered contains 8×8 coarse cells and is illustrated by the lines in the plot. We note that the MMMFEM-PBS solution is more accurate than the MMMFEM-POL.

4.3.2. The MHM for permeability fields with barriers

In the next experiment, the same problem of the previous subsection is considered, except that the fractures are replaced by barriers of low permeability. The physics-based flux space is used at interfaces that contain cells in which the absolute permeability is lower than a cutoff value ζ_{\min} . We combine the flux space with the MHM to approximate the solution. Similar to the previous example, we compare different permeability contrasts. Here, we consider the permeability in the barrier, K_{\min} varying from 10^{-8} to 10^{-1} whereas the background is homogeneous with $K = 1$, see Figure 9 (a). The cutoff value set to capture the barriers is $\zeta_{\min} = 1$ in all cases. The relative $L^2(\Omega)$ errors for flux as function of the contrast are displayed in Figure 9 (b). Similar to the previous case, the solution is more accurate by using the physics-based space instead of the linear space. The flux errors provided by the linear spaces increase quickly with the contrast whereas the errors from the physics-based spaces are controlled. The results are consistent for the three domain decompositions, where the smaller errors are provided by the decompositions with more subdomains. In Figure 10 we show the flux approximations for the decomposition of 8×8 coarse cells in the highest permeability contrast $K_{\max}/K_{\min} = 10^8$. We note that the MHM-POL solution is inaccurate and the MHM-PBS approximation captures the correct behavior of the reference solution.

5. Adaptive MRCM with the physics-based interface spaces

We can conclude from the numerical studies reported above that the physics-based pressure (respectively, flux) space is fundamental to produce an accurate pressure (resp., flux) solution in presence of fractures (resp., barriers). Therefore if fractures and barriers appear in a single interface one can achieve a better approximation of pressure and flux using both pressure and flux physics-based interface spaces. To attain this goal one feature necessary for the multiscale method used is the ability to include the interface spaces independently. For this purpose, we combine the physics-based interface spaces with the MRCM, whose formulation enables to include the spaces separately. In the MRCM framework, we consider the adaptive version (denoting by *a*MRCM) that consists of setting the function $\alpha(\mathbf{x})$ depending on the variation of the permeability field at the interfaces. In a previous work [28], we found that the best choice is to set a small value α_{small} (pressure is favored) for regions where the permeability is larger than a cutoff value and

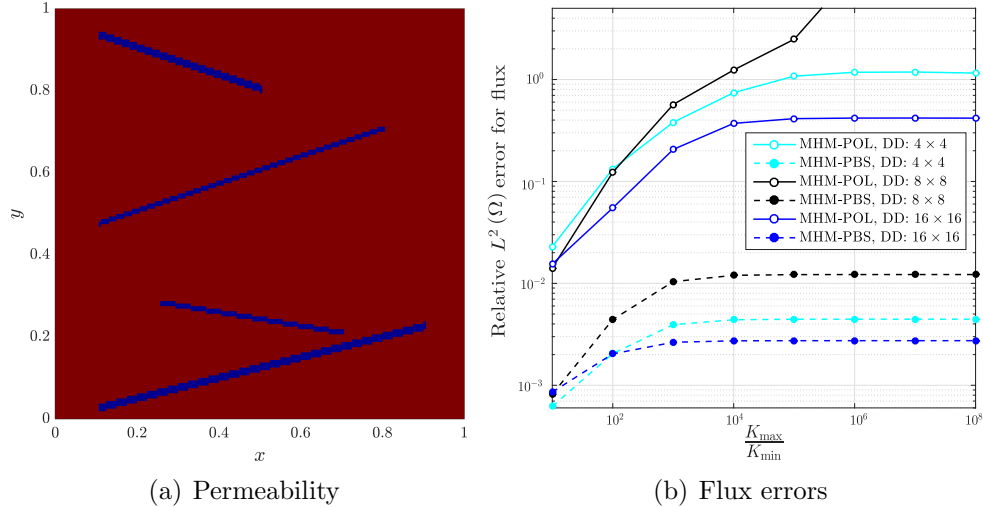


Figure 9: High-contrast permeability field with barriers (a). We consider the permeability in the barrier, K_{\min} varying from 10^{-8} to 10^{-1} whereas the background is homogeneous with $K = 1$. Relative $L^2(\Omega)$ flux errors as function of the contrast are shown for the MHM-POL and MHM-PBS (b). Three domain decompositions are considered: with 4×4 , 8×8 and 16×16 coarse cells. We note that for high-contrast the only accurate approximations are produced by the MHM-PBS (in all the meshes).

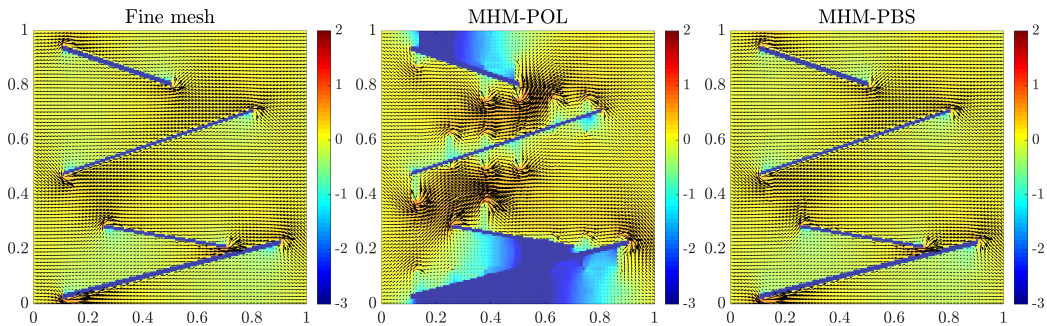


Figure 10: Flux approximations considering the contrast of $K_{\max}/K_{\min} = 10^8$. Left to right: fine mesh, MHM-POL, and MHM-PBS solutions. The colors in the flux plot refer to the log-scale flux magnitude. The domain decomposition considered contains 8×8 coarse cells and is illustrated by the lines in the plot. We note that the MHM-PBS approximation is closely related to the reference solution and the MHM-POL is inaccurate.

a large value α_{large} (flux is favored) for the remaining areas. In this sense, the a MRCM controls the relative importance of each interface space at each location.

To solve the Equations (1) or (2) by the MRCM we need to set the interface parameters (i.e., the interface spaces and the adaptive function $\alpha(\mathbf{x})$). In Algorithm 1 we detail the preprocessing operations to set the interface spaces and the adaptive coefficient $\alpha(\mathbf{x})$ from the permeability field. At each interface Γ_k , $k = 1, \dots, M$ (where M is the total number of interfaces, horizontal or vertical), and at each interface cell $e_l \in \Gamma_k$, $l = 1, \dots, m_k$ (where m_k is the number of fine cells in Γ_k), it is defined whether e_l corresponds to a fracture, a barrier, or to background, and then $\alpha(\mathbf{x}_l)$ (at the cell's center) is set accordingly. Then, we use the proposed physics-based interface spaces taking into account the observations presented in the previous section. We set the interface pressure (resp., flux) spaces $\mathcal{P}_{H,1}^*$ (respectively, $\mathcal{U}_{H,1}^*$) that consider the physics-based space for the interfaces containing fractures (resp., barriers) and linear spaces for the remaining interfaces. Finally we are able to combine the a MRCM with the physics-based spaces ($\mathcal{U}_{H,1}^*, \mathcal{P}_{H,1}^*$). We refer to this combination as a MRCM-PBS and consider for comparisons, the a MRCM-POL, which represents the a MRCM combined with linear polynomial spaces independently on the permeability field.

In the next section, we explore the proposed a MRCM-PBS in challenging high-contrast fractured-like porous media through numerical experiments.

6. Numerical experiments

We present representative numerical experiments to investigate the accuracy of the introduced physics-based interface spaces for the approximation of flows in high-contrast fractured-like porous media. We start with the investigation of the physics-based interface spaces combined with the a MRCM for the elliptic problem. Then we study the influence of the physics-based interface spaces in the approximation of two-phase problems.

In all simulations the fine grid solution is used as the reference solution for evaluating the multiscale approximations. We consider the a MRCM (by setting $\alpha_{\text{small}} = 10^{-2}$ and $\alpha_{\text{large}} = 10^2$), MMMFEM (by setting $\alpha = 10^{-6}$) and MHM (by setting $\alpha = 10^6$). To recover a continuous flux at the fine-scale we consider a velocity post-processing (downscaling) [57]. We choose the Stitch method, which has been indicated as the procedure that provides the best compromise between computational cost and precision. The patch

Algorithm 1 Setting interface parameters for solving Equations (1) or (2) by the *a*MRCM-PBS

```

1: Given  $K(\mathbf{x})$ ,  $\zeta_{\min}$ ,  $\zeta_{\max}$ ,  $\alpha_{\text{small}}$  and  $\alpha_{\text{large}}$ 
2: for  $k = 1$  to  $M$  do
3:   for  $l = 1$  to  $m_k$  do
4:     Evaluate the permeability in both sides ( $K^-(\mathbf{x}_l)$  and  $K^+(\mathbf{x}_l)$ ) of the
     interface cell  $e_l \in \Gamma_k$ 
5:     if ( $\max\{K^-(\mathbf{x}_l), K^+(\mathbf{x}_l)\} > \zeta_{\max}$ ) then
6:        $\alpha(\mathbf{x}_l) = \alpha_{\text{small}}$ 
7:       Add  $\Gamma_k$  to  $\Gamma^{\text{frac}}$ 
8:     else
9:        $\alpha(\mathbf{x}_l) = \alpha_{\text{large}}$ 
10:    end if
11:    if ( $\min\{K^-(\mathbf{x}_l), K^+(\mathbf{x}_l)\} < \zeta_{\min}$ ) then
12:      Add  $\Gamma_k$  to  $\Gamma^{\text{barrier}}$ 
13:    end if
14:  end for
15:  if ( $\Gamma_k \subset \Gamma^{\text{frac}}$ ) then
16:    Compute the physics-based functions for pressure from Equations
    (13)-(15)
17:    Set  $\mathcal{P}_{H,1}^* = \mathcal{P}_H^*$  at  $\Gamma_k$ 
18:  else
19:    Compute the linear polynomials functions for pressure
20:    Set  $\mathcal{P}_{H,1}^* = \mathcal{P}_{H,1}$  at  $\Gamma_k$ 
21:  end if
22:  if ( $\Gamma_k \subset \Gamma^{\text{barrier}}$ ) then
23:    Compute the physics-based functions for flux from Equations (16)-
    (18)
24:    Set  $\mathcal{U}_{H,1}^* = \mathcal{U}_H^*$  at  $\Gamma_k$ 
25:  else
26:    Compute the linear polynomials functions for flux
27:    Set  $\mathcal{U}_{H,1}^* = \mathcal{U}_{H,1}$  at  $\Gamma_k$ 
28:  end if
29: end for
30: Given  $(\mathcal{U}_{H,1}^*, \mathcal{P}_{H,1}^*)$  and  $\alpha(\mathbf{x})$ , solve Equations (1) or (2) to obtain  $p(\mathbf{x})$ 
    and  $\mathbf{u}(\mathbf{x})$  by the aMRCM-PBS

```

thicknesses of the oversampling regions for the Stitch method is fixed in two elements (that represents 10% of the size of most subdomains considered in the examples).

6.1. Single-phase flows in permeability fields with fractures and barriers

We consider a permeability field containing both fractures and barriers, see Figure 11. We fix the homogeneous background permeability with $K = 1$ and consider the permeability in the barriers, K_{\min} varying from 10^{-4} to 0.5 whereas the permeability in the fractures, K_{\max} varying from 10 to 10^4 . The cutoff values considered are $\zeta_{\max} = \zeta_{\min} = 1$.

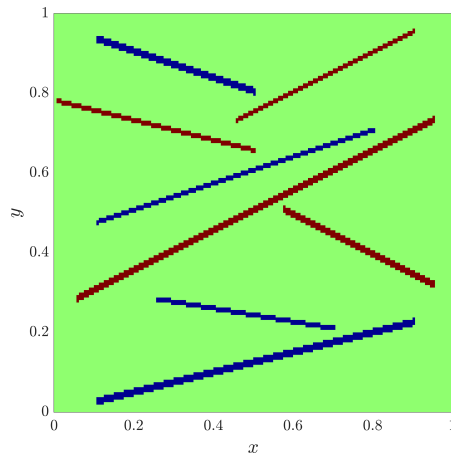


Figure 11: Permeability field containing both fractures (red) and barriers (blue). The contrast considered vary from 10 to 10^8 .

The relative $L^2(\Omega)$ error norms for pressure and flux as function of the contrast are shown in Figure 12 for three domain decompositions: with 4×4 , 8×8 and 16×16 coarse cells. We observe that the pressure and flux errors related to the linear interface spaces increase quickly with the contrast. However, the errors provided by the physics-based spaces are moderate even for very large permeability contrasts. The results are consistent for all the domain decomposition tested, where the smaller errors are attained by the decompositions with more subdomains. In Figure 13 we compare the solutions provided by the *a*MRCM, MMMFEM and MHM considering the domain decomposition of 8×8 subdomains having 20×20 fine cells into each one. The first observation is that the MMMFEM and MHM approximations are not accurate for the permeability field with fractures and barriers even using

the physics-based interface spaces. On the other hand, the a MRCM-PBS solutions are expressively more accurate than the ones obtained with the a MRCM-POL. The pressure and flux approximations for the permeability contrast of 10^8 are shown in Figure 14 and Figure 15, respectively. The plots confirm that the a MRCM combined with the physics-based interface spaces produces the most accurate solutions. We observe that all methods fail when using the linear interface spaces. We can conclude that the physics-based interface spaces are indispensable for a reasonable approximation of pressure, flux and further applications in two-phase flows.

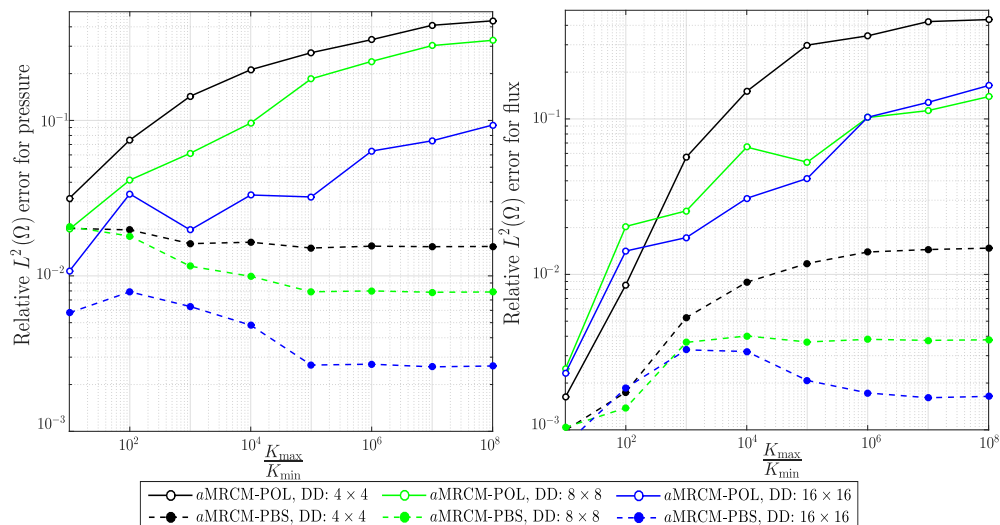


Figure 12: Relative $L^2(\Omega)$ pressure (left) and flux (right) errors as function of the contrast are shown for the a MRCM-POL and a MRCM-PBS. Three domain decompositions are considered: with 4×4 , 8×8 and 16×16 coarse cells. We note that the a MRCM-PBS is more accurate than the a MRCM-POL in all the contrast and meshes considered.

Finally, we present in Figure 16 the behavior of the errors for pressure and flux as a function of α (varying from 10^{-6} to 10^6) for the permeability contrast of 10^8 and maintaining the domain decomposition of 8×8 coarse cells. We compare the MRCM errors with linear and physics-based interface spaces. Two choices for the a MRCM are presented: setting $\alpha_{\text{small}} = 10^{-2}$ and $\alpha_{\text{large}} = 10^2$ or $\alpha_{\text{small}} = 10^{-6}$ and $\alpha_{\text{large}} = 10^6$. The errors for the adaptive version of the MRCM are illustrated as horizontal lines. We note a strong dependence on the parameter α , where the minimum errors are attained at

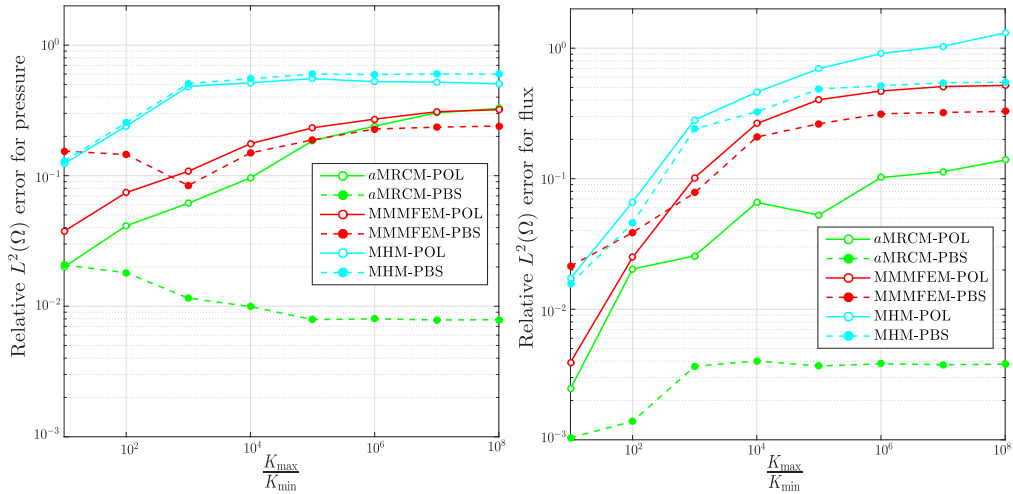


Figure 13: Relative $L^2(\Omega)$ pressure (left) and flux (right) errors as function of the contrast are shown for the a MRCM, MMMFEM and MHM considering both the linear and physics-based spaces. Three domain decompositions are considered: with 4×4 , 8×8 and 16×16 coarse cells. We note that the a MRCM-PBS is more accurate than the a MRCM-POL in all the contrast and meshes considered.

intermediate values (for choosing α constant), similarly to the previous works [27, 17, 28]. But the approximations by choosing any constant value of α , even for the MRCM-PBS are inaccurate. We remark that the MMMFEM and MHM are also included in this observation. One can conclude that, besides the physics-based interface spaces, the a MRCM is necessary to obtain more accurate solutions. We note that the choice of $\alpha_{\text{small}} = 10^{-2}$ and $\alpha_{\text{large}} = 10^2$ or $\alpha_{\text{small}} = 10^{-6}$ and $\alpha_{\text{large}} = 10^6$ does not affect significantly the error.

These results indicate that the linear interface spaces are not robust for capturing the effects of features as fractures and barriers. Even the physics-based spaces are not enough for complex fields if not combined with an appropriate multiscale method. In order to study how these results are reflected in the corresponding saturation fields, in the next subsection we present numerical results for two-phase flows.

6.2. Two-phase flow and transport problems

Now we focus on a study of the MRCM performance for two-phase flows using the physics-based interface spaces for high-contrast fractured-like permeability fields. We introduce the saturation comparisons with a detailed

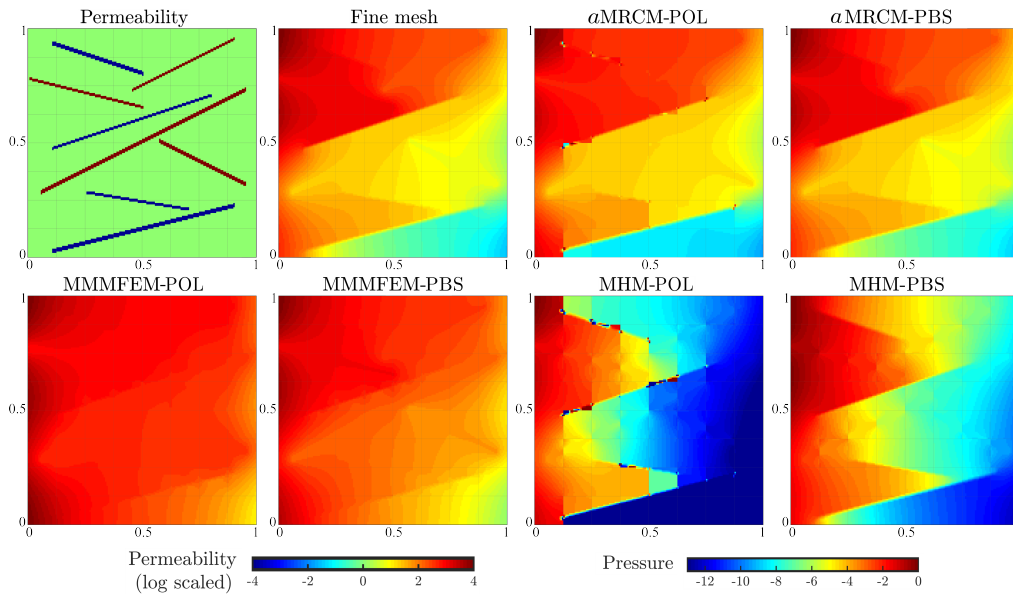


Figure 14: Pressure approximations considering the contrast of $K_{\max}/K_{\min} = 10^8$. First line, left to right: permeability field, fine mesh, a MRCM-POL, and a MRCM-PBS solutions. Second line, left to right: MMMFEM-POL, MMMFEM-PBS, MHM-POL, and MHM-PBS solutions. The domain decomposition considered contains 8×8 coarse cells and is illustrated by the lines in the plot. We note that the a MRCM-PBS approximation is the most closely related to the reference solution followed by the a MRCM-POL.

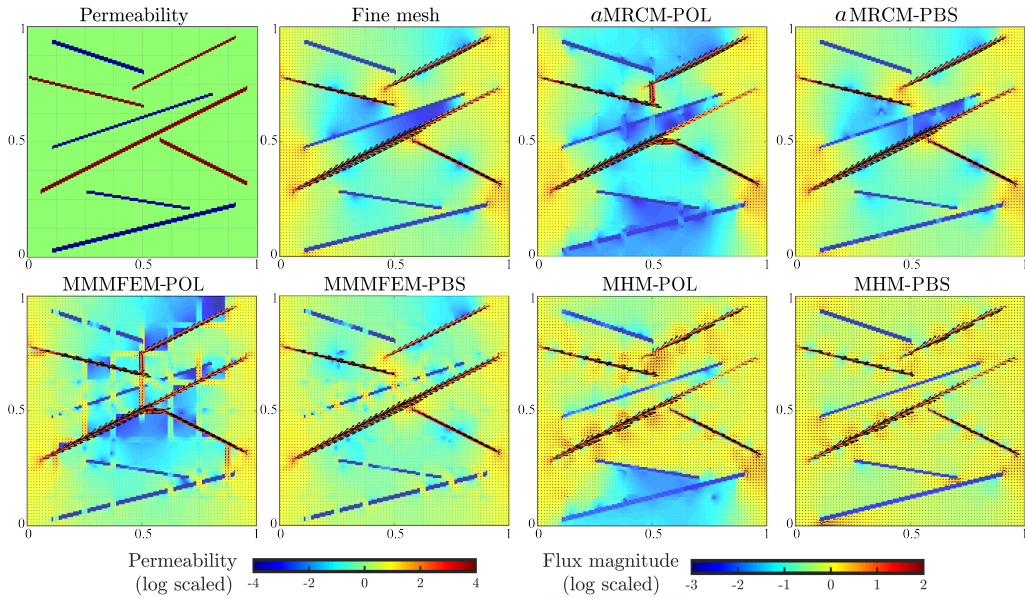


Figure 15: Flux approximations considering the contrast of $K_{\max}/K_{\min} = 10^8$. First line, left to right: permeability field, fine mesh, a MRCM-POL, and a MRCM-PBS solutions. Second line, left to right: MMMFEM-POL, MMMFEM-PBS, MHM-POL, and MHM-PBS solutions. The colors refer to the log-scale flux magnitude. The domain decomposition considered contains 8×8 coarse cells and is illustrated by the lines in the plot. The only accurate procedure is the a MRCM-PBS.

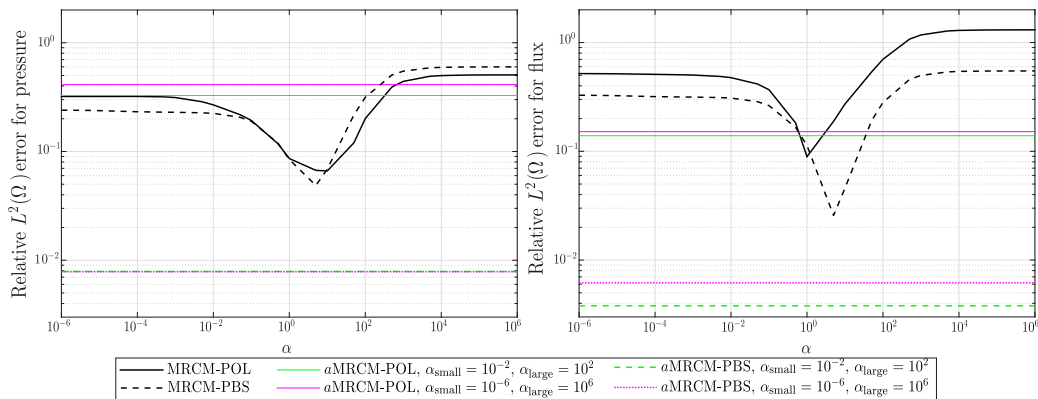


Figure 16: Relative $L^2(\Omega)$ errors as a function of α for pressure (left) and flux (right) considering the permeability field plotted in Figure 11 with contrast of 10^8 and the domain decomposition that contains 8×8 coarse cells. The physics-based and linear spaces are compared. We include the errors for two choices in the a MRCM: setting $\alpha_{\text{small}} = 10^{-2}$ and $\alpha_{\text{large}} = 10^2$ or $\alpha_{\text{small}} = 10^{-6}$ and $\alpha_{\text{large}} = 10^6$ (illustrated as horizontal lines). The improvement with the combination of the a MRCM and the physics-based spaces is expressive.

analysis of fingering instabilities to show the impact of the design of the basis functions on the transport of the water saturation. Firstly we present numerical results for the permeability field with fractures and barriers of the previous section. Then we consider a high-contrast permeability field with channels and isolated inclusions that has frequently appeared in the literature [58].

In all simulations the reservoir is initially filled with oil ($s^0 = 0$) and water is injected at a constant rate. The relative permeabilities are given by $k_{ro} = (1 - s)^2$ and $k_{rw} = s^2$, such that the fractional flow is written as

$$f(s) = \frac{Ms^2}{Ms^2 + (1 - s)^2}, \quad (19)$$

where $M = \mu_o/\mu_w$ is set as $M = 10$.

In the operator splitting approach, we take the number of transport steps between the elliptic updates at most $C = 20$. The time units employed are in pore volumes injected (PVI) that refers to the fraction of the total accessible pore volume injected into the domain [1]

$$T_{\text{PVI}} = -V_p^{-1} \int_0^t \int_{\partial\Omega_{\text{in}}} \mathbf{u}(\mathbf{x}, \tau) \cdot \mathbf{n} \, dl \, d\tau, \quad (20)$$

where V_p is the total pore-volume of the reservoir, t is the time taken for injection and $\partial\Omega_{\text{in}}$ the inflow well boundaries with the outward unit normal \mathbf{n} .

6.2.1. High-contrast permeability field with fractures and barriers

The objective of this study is to investigate the a MRCM, MMMFEM and MHM saturation solutions considering the physics-based interface spaces for the high-contrast permeability field with fractures and barriers. We consider the permeability field of the previous experiment, illustrated in Figure 11. We fix the highest permeability contrast $K_{\text{max}}/K_{\text{min}} = 10^8$ and the domain decomposition having 8×8 subdomains, each one discretized by 20×20 cells.

The first example considers the same slab geometry of the previous experiments, by imposing the flux on the left and right boundaries and no source terms. Figure 17 shows the permeability field (log-scaled) along with the saturation profiles at $T_{\text{PVI}} = 0.06$ (before breakthrough time) approximated by the multiscale methods with the linear and the physics-based interface spaces. The procedure that produces a saturation solution closer to the reference one is the a MRCM-PBS. The use of the physics-based spaces enables more accurate solutions for the a MRCM and the MMMFEM. However, the last one is still inaccurate. The MHM solutions are unacceptable either for linear or physics-based spaces. The corresponding relative $L^1(\Omega)$ errors throughout the simulation are presented in Figure 18. We note an expressive improvement provided by the physics-based interface spaces combined with the a MRCM. This combination enables the error to drop by one order of magnitude.

Now we maintain the slab geometry but using global boundary conditions of no-flow at top and bottom boundaries along with imposed pressure on the left and right boundaries. In Figure 19 we present the saturation profiles at $T_{\text{PVI}} = 0.0001$ (before breakthrough time) approximated by the multiscale methods with the linear and the physics-based interface spaces. Similar results to the previous example are obtained. The corresponding relative errors throughout the simulation are presented in Figure 20, where it is clear the improved accuracy provided by combining the physics-based spaces with the a MRCM. Again, the MHM solutions are not acceptable with both interface spaces. The MMMFEM approximations improve significantly with the physics-based spaces, however, these solutions are comparable to the a MRCM-POL approximations.

Lastly, we test the multiscale methods in a quarter of a five-spot model,

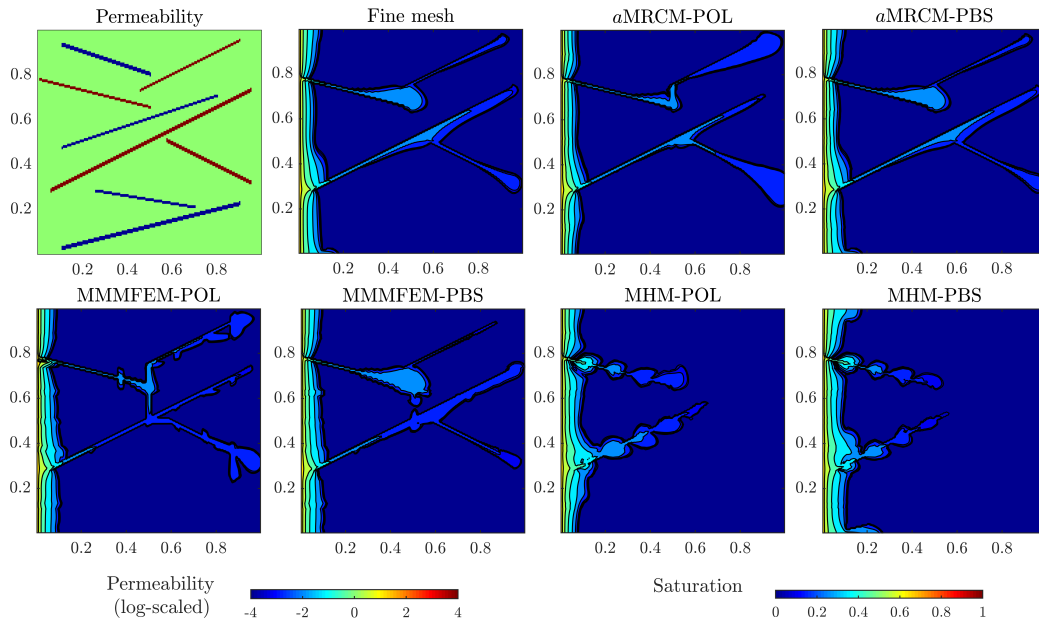


Figure 17: Comparison of multiscale methods for the slab geometry with flux boundary conditions on the left and right. Saturation profiles at $T_{PVI} = 0.06$ for the permeability field with fractures and barriers are shown. First line, left to right: high-contrast permeability field (log-scaled); reference fine grid solution; a MRCM-POL saturation profile; a MRCM-PBS saturation profile. Second line, left to right: MMMFEM-POL saturation profile; MMMFEM-PBS saturation profile; MHM-POL saturation profile; MHM-PBS saturation profile. The a MRCM-PBS provides the most accurate approximation.

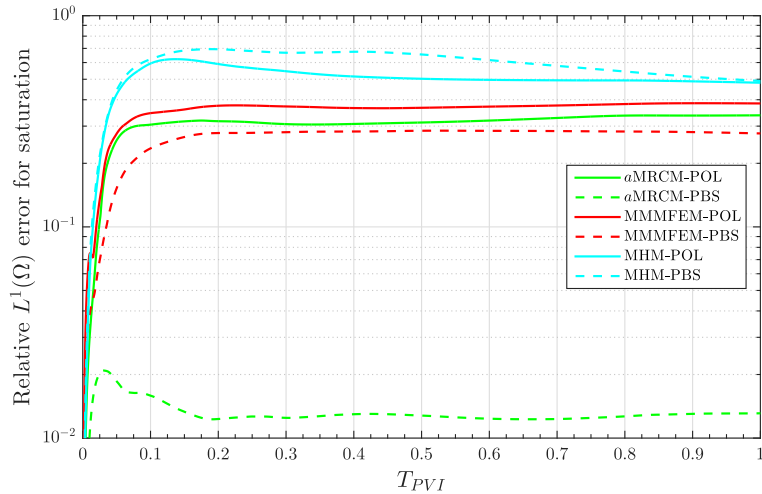


Figure 18: Relative $L^1(\Omega)$ saturation errors as a function of time for the slab geometry with flux boundary conditions considering the field with fractures and barriers. We compare the a MRCM, MMMFEM and MHM with both physics-based and linear spaces. We note that the errors associated with the a MRCM-PBS are much smaller than all the others.

where we inject the water at the bottom-left cell and the sink is located at the top-right cell. The saturation profiles at $T_{PVI} = 0.09$ (before breakthrough time) are shown in Figure 21. The most accurate solutions are produced by the a MRCM considering both types of interface spaces. The MMMFEM and MHM approximations present expressive fingering instabilities that are not present in the fine grid solution. In Figure 22, the relative errors confirm that the a MRCM produces more accurate solutions. It is noticeable the poor quality solutions provided by the MMMFEM and MHM (even with the physics-based spaces), that are less accurate than the a MRCM-POL approximation. The solutions produced by the a MRCM-PBS are much more accurate than all the other approximations.

The high-contrast permeability fields are challenging for multiscale methods. We show that the methods fail in a field with both fractures and barriers. In all the models previously tested, the a MRCM-PBS is the only scheme that provides satisfactory approximations.

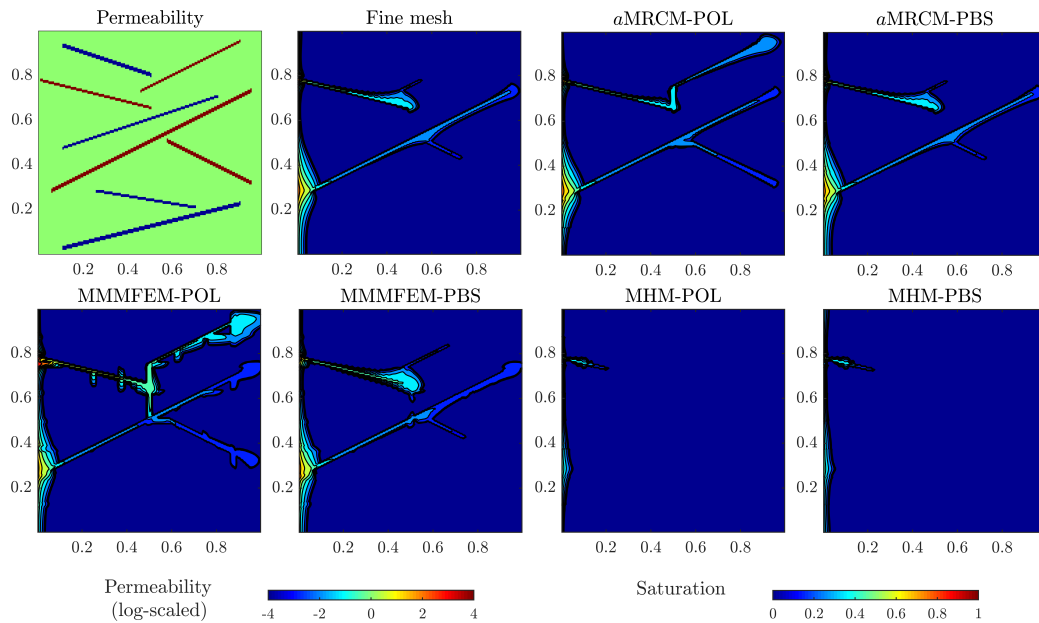


Figure 19: Comparison of multiscale methods for the slab geometry with pressure boundary conditions on the left and right. Saturation profiles at $T_{PVI} = 0.0001$ for the permeability field with fractures and barriers are shown. First line, left to right: high-contrast permeability field (log-scaled); reference fine grid solution; *a*MRCM-POL saturation profile; *a*MRCM-PBS saturation profile. Second line, left to right: MMMFEM-POL saturation profile; MMMFEM-PBS saturation profile; MHM-POL saturation profile; MHM-PBS saturation profile. The *a*MRCM-PBS is clearly the most accurate procedure.

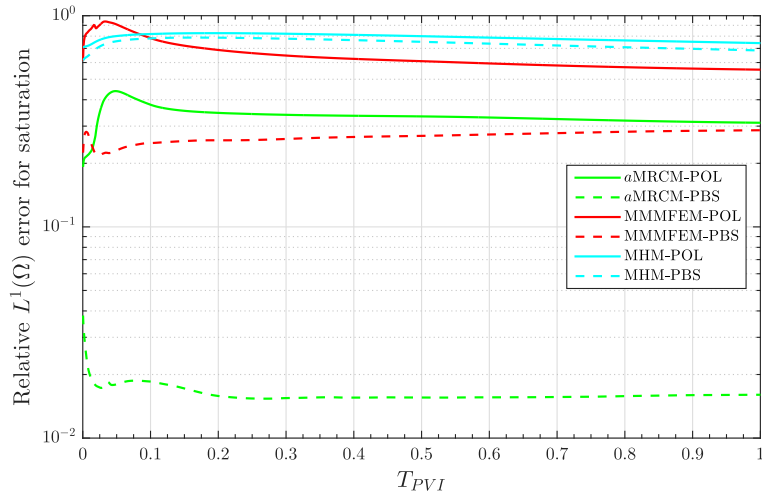


Figure 20: Relative $L^1(\Omega)$ saturation errors as a function of time for the slab geometry with pressure boundary conditions considering the field with fractures and barriers. We compare the a MRCM, MMMFEM and MHM with both physics-based and linear spaces. Similarly to the previous example, the errors associated with the a MRCM-PBS are much smaller than all the others.

6.2.2. High-contrast permeability field with channels and isolated inclusions

In this subsection, we consider a high-contrast permeability field with channels and isolated inclusions that has frequently appeared in the literature [7, 13, 15, 14, 19, 20, 58]. We consider a domain Ω containing 100×100 fine grid cells divided into 5×5 subdomains. The boundary conditions are no-flow at the top and bottom boundaries along with an imposed flux on the left and right boundaries. No source terms are considered. The permeability contrast considered is $K_{\max}/K_{\min} = 10^6$ and the cutoff values are set as $\zeta_{\max} = \zeta_{\min} = 1$.

Figure 23 shows the permeability field (log-scaled) containing high-permeable channels and isolated inclusions and the saturation profiles at $T_{PVI} = 0.07$ (before breakthrough). In this example, only the pressure physics-based spaces are used to handle the high-permeable structures, since there are no barriers. The more accurate solutions are provided by the a MRCM-PBS and the MMMFEM-PBS. For these two methods, the figure shows that the imprecisions that happen by using the linear spaces have completely disappeared with the physics-based spaces. The MHM solutions are inaccurate. We remark that the MHM provides the same solution with the linear and

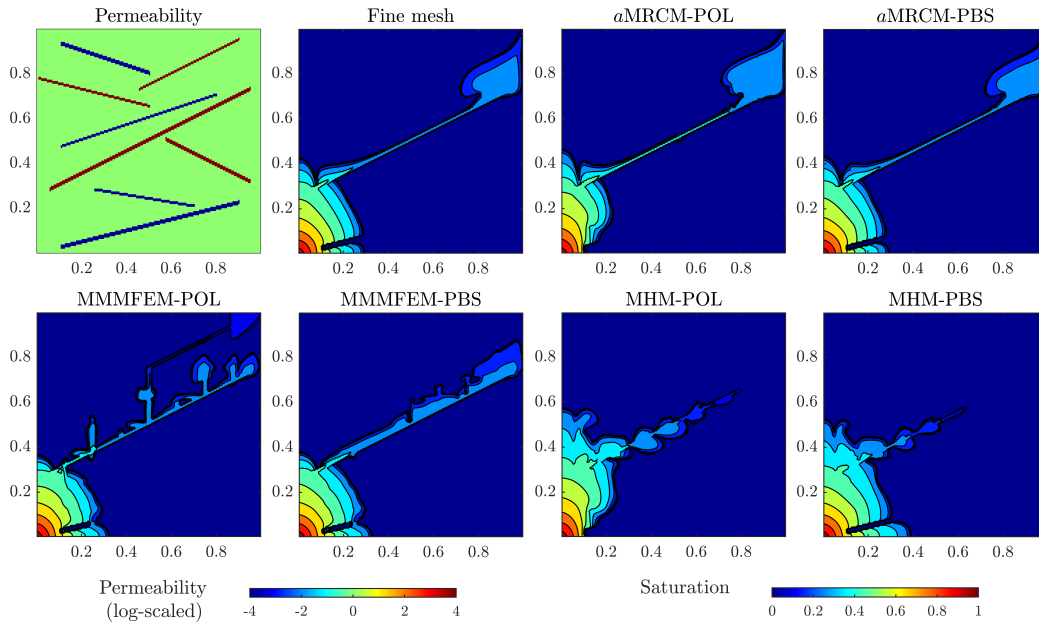


Figure 21: Comparison of multiscale methods for the quarter of a five-spot geometry. Saturation profiles at $T_{PVI} = 0.09$ for the permeability field with fractures and barriers are shown. First line, left to right: high-contrast permeability field (log-scaled); reference fine grid solution; a MRCM-POL saturation profile; a MRCM-PBS saturation profile. Second line, left to right: MMMFEM-POL saturation profile; MMMFEM-PBS saturation profile; MHM-POL saturation profile; MHM-PBS saturation profile. The a MRCM is the only procedure that captures the details of the fingers.

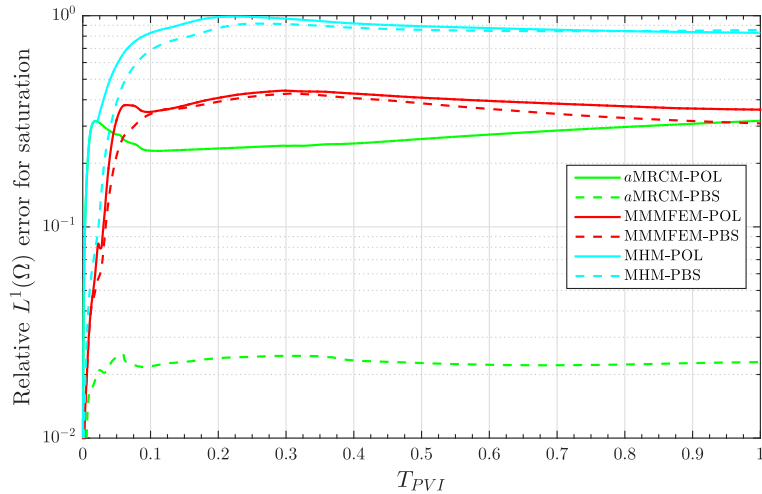


Figure 22: Relative $L^1(\Omega)$ saturation errors as a function of time for the quarter of a five-spot geometry on the field with fractures and barriers. We compare the $aMRCM$, $MMMFEM$ and MHM with both physics-based and linear spaces. The errors associated with the $aMRCM-PBS$ are the smallest, followed by the $aMRCM-POL$.

the physics-based interface spaces, because this method considers only the flux space, which is always maintained as linear for this permeability field. The relative errors are shown in Figure 24 and reflect these observations throughout the whole simulation.

As a final validation, we consider the performance of the methods in dealing with the same high-contrast permeability field replacing the type of channelized structures to barriers, as in [58]. Figure 25 shows the permeability field (log-scaled) containing the low-permeable channels and the saturation profiles at $T_{PVI} = 0.33$ (before breakthrough). In this case, only the flux physics-based spaces are used, since there are only low-permeable structures. We note a considerable improvement in the $aMRCM$ and MHM approximations replacing the linear interface spaces by the physics-based ones. The $MMMFEM$ solutions present just some modest errors if compared to the $aMRCM-POL$ and $MHM-POL$ approximations. We remark that the $MMMFEM$ solutions are the same with the linear and the physics-based interface spaces because, this method considers only the pressure space, which is always maintained as linear for this permeability field. The relative errors throughout the whole simulation are shown in Figure 26. We confirm that

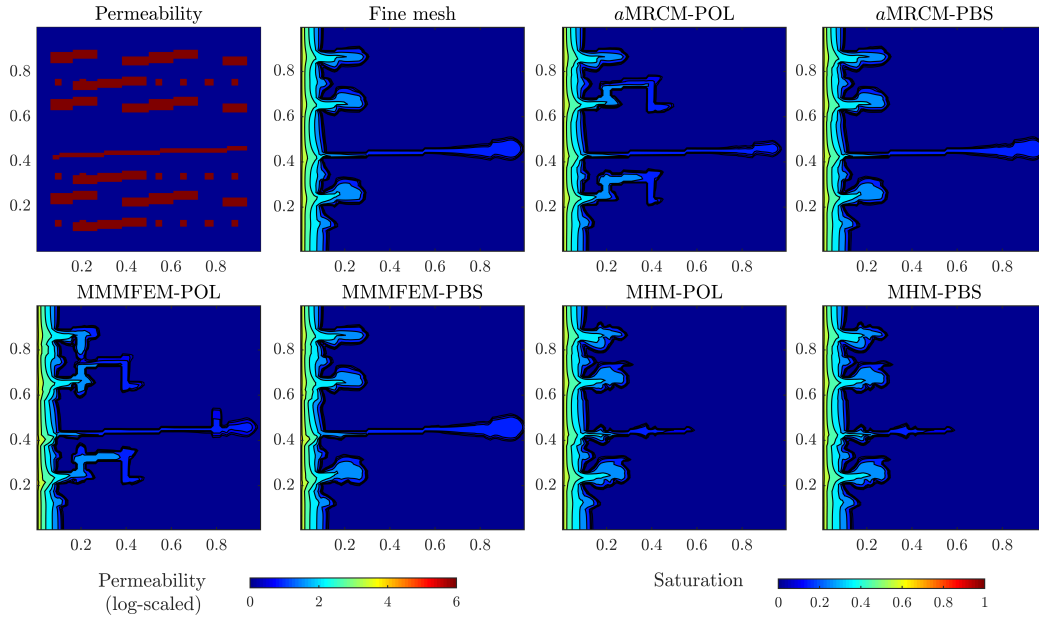


Figure 23: Comparison of multiscale methods. Saturation profiles at $T_{PVI} = 0.07$ for the permeability field with channels and isolated inclusions. First line, left to right: high-contrast permeability field (log-scaled); reference fine grid solution; a MRCM-POL saturation profile; a MRCM-PBS saturation profile. Second line, left to right: MMMFEM-POL saturation profile; MMMFEM-PBS saturation profile; MHM-POL saturation profile; MHM-PBS saturation profile. The more accurate approximations are attained by the a MRCM-PBS and MMMFEM-PBS.

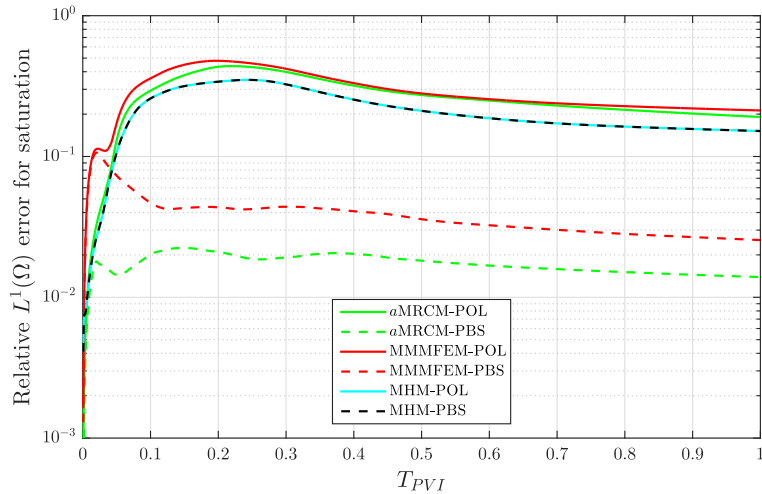


Figure 24: Relative $L^1(\Omega)$ saturation errors as a function of time on the field with channels and isolated inclusions. We compare the $aMRCM$, $MMMFEM$ and MHM with both physics-based and linear spaces. The errors associated with the $aMRCM-PBS$ and $MMMFEM-PBS$ are the smallest.

the $aMRCM-POL$ and $MHM-POL$ are not accurate, the $MMMFEM$ provides intermediate results and the $aMRCM-PBS$ and $MHM-PBS$ produce the most accurate approximations.

The numerical studies demonstrate the improvement obtained by using physics-based interface spaces. High-contrast fields were chosen that allowed us to assess the ability of the methods to handle problems in the presence of both high and low-permeable structures. The results provide strong evidence that the adaptive $MRCM$ combined with the physics-based spaces leads to improved transport approximations in high-contrast fractured-like porous media.

7. Conclusions

Two physics-based interface spaces (one for pressure and other for flux) have been proposed for better capturing the high-contrast effects of channelized structures. A careful investigation has been performed for the numerical solution of single and two-phase flows by combining the new spaces with multiscale mixed methods.

We show that the introduced physics-based pressure space can offer much better accuracy in comparison with the usual polynomial spaces in the pres-

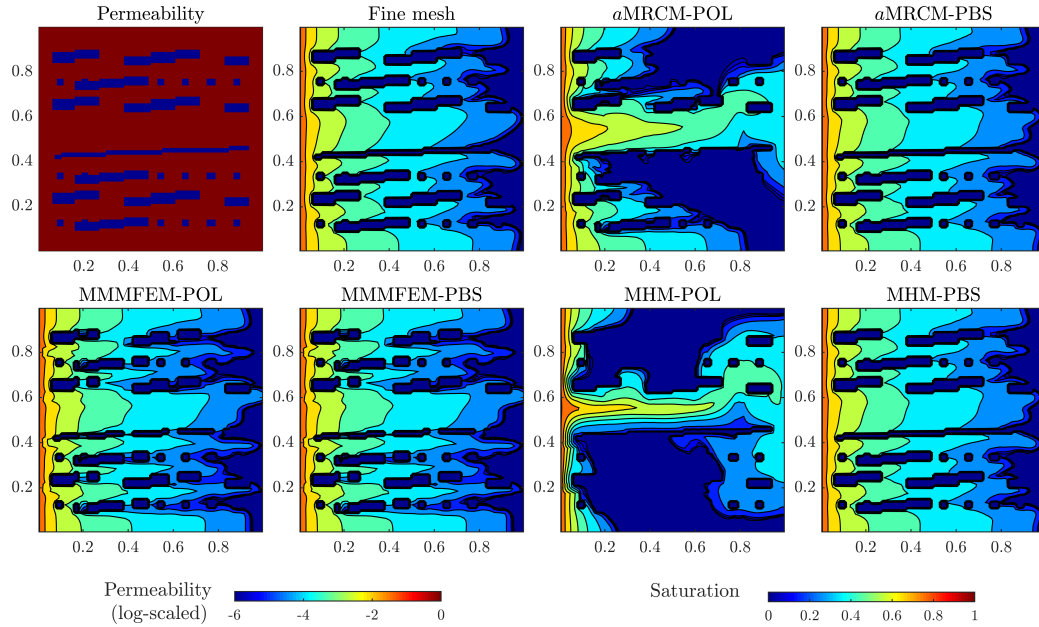


Figure 25: Comparison of multiscale methods. Saturation profiles at $T_{PVI} = 0.33$ for the permeability field with barriers are shown. First line, left to right: high-contrast permeability field (log-scaled); reference fine grid solution; $aMRCM-POL$ saturation profile; $aMRCM-PBS$ saturation profile. Second line, left to right: $MMMFEM-POL$ saturation profile; $MMMFEM-PBS$ saturation profile; $MHM-POL$ saturation profile; $MHM-PBS$ saturation profile. A considerable improvement is noticed in the $aMRCM$ and MHM approximations replacing the linear spaces by the physics-based.

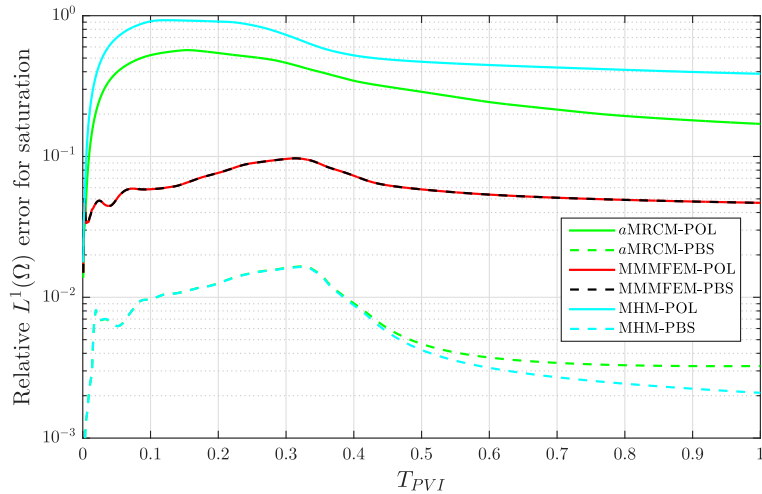


Figure 26: Relative $L^1(\Omega)$ saturation errors as a function of time on the field with barriers. We compare the a MRCM, MMMFEM and MHM with both physics-based and linear spaces. The a MRCM-PBS and MMMFEM-PBS produce the smallest errors.

ence of high-permeable structures. On the other hand, the proposed physics-based flux space can provide more accurate solutions in comparison with the polynomial spaces in the presence of low-permeable structures. Two well known multiscale procedures have been applied to confirm these results: the Multiscale Mortar Mixed Finite Element Method (combined with the pressure space) and the Multiscale Hybrid-Mixed Finite Element Method (using the flux space). Aiming at using simultaneously both interface spaces we combine them with the MRCM, which allows for including the interface spaces independently. With this combination, we achieve the best accuracy in the approximation of challenging high-contrast flows in comparison with the other multiscale methods tested.

The MRCM formulation can take advantage of parallel computations with a computational cost comparable to existing procedures and providing a superior accuracy of the solutions in challenging high-contrast fields than the other multiscale methods that we have considered. The development of interface spaces based on physics for 3D reservoir flow problems is outside the scope of the work presented here. However, this is a topic that is currently being considered by the authors. Future work may include the use of the MRCM in more complex flow models, including the implicit solution of

multiphase flow and transport problems.

Acknowledgments

The authors gratefully acknowledge the financial support received from the Brazilian oil company Petrobras grant 2015/00400-4, and from the São Paulo Research Foundation FAPESP grant CEPID-CeMEAI 2013/07375-0; This study was also financed in part by Brazilian government agencies CAPES (Finance Code 001) and CNPq grants 305599/2017-8 and 310990/2019-0; FP was also funded in part by NSF-DMS 1514808, a Science Without Borders/CNPq-Brazil grant 400169/2014-2 and UT Dallas; FFR acknowledges the hospitality provided by UT Dallas; Finally, the authors thank R.T. Guiraldello for providing the MRCM code and for fruitful discussions about the method.

References

- [1] Z. Chen, G. Huan, Y. Ma, Computational methods for multiphase flows in porous media, Vol. 2, SIAM, 2006.
- [2] V. Kippe, J. E. Aarnes, K. Lie, A comparison of multiscale methods for elliptic problems in porous media flow, *Computational Geosciences* 12 (3) (2008) 377–398.
- [3] P. Jenny, S. Lee, H. A. Tchelepi, Multi-scale finite-volume method for elliptic problems in subsurface flow simulation, *Journal of Computational Physics* 187 (1) (2003) 47–67.
- [4] P. Jenny, S. H. Lee, H. A. Tchelepi, Adaptive multiscale finite-volume method for multiphase flow and transport in porous media, *Multiscale Modeling & Simulation* 3 (1) (2005) 50–64.
- [5] T. Hou, X.-H. Wu, A multiscale finite element method for elliptic problems in composite materials and porous media, *Journal of Computational Physics* 134 (1997) 169–189.
- [6] J. E. Aarnes, T. Y. Hou, Multiscale domain decomposition methods for elliptic problems with high aspect ratios, *Acta Mathematicae Applicatae Sinica* 18 (1) (2002) 63–76.

- [7] Y. Efendiev, J. Galvis, T. Y. Hou, Generalized multiscale finite element methods (GMsFEM), *Journal of Computational Physics* 251 (2013) 116–135.
- [8] Z. Chen, T. Hou, A mixed multiscale finite element method for elliptic problems with oscillating coefficients, *Mathematics of Computation* 72 (2003) 541–576.
- [9] J. E. Aarnes, On the use of a mixed multiscale finite element method for greater flexibility and increased speed or improved accuracy in reservoir simulation, *Multiscale Modeling & Simulation* 2 (3) (2006) 421–439.
- [10] T. Arbogast, G. Pencheva, M. Wheeler, I. Yotov, A multiscale mortar mixed finite element method, *Multiscale Modeling & Simulation* 6 (1) (2007) 319–346.
- [11] C. Harder, D. Paredes, F. Valentin, A family of multiscale hybrid-mixed finite element methods for the Darcy equation with rough coefficients, *Journal of Computational Physics* 245 (2013) 107–130.
- [12] A. Francisco, V. Ginting, F. Pereira, J. Rigelo, Design and implementation of a multiscale mixed method based on a nonoverlapping domain decomposition procedure, *Mathematics and Computers in Simulation* 99 (2014) 125–138.
- [13] E. T. Chung, Y. Efendiev, C. S. Lee, Mixed generalized multiscale finite element methods and applications, *Multiscale Modeling & Simulation* 13 (1) (2015) 338–366.
- [14] E. T. Chung, Y. Efendiev, G. Li, An adaptive GMsFEM for high-contrast flow problems, *Journal of Computational Physics* 273 (2014) 54–76.
- [15] E. T. Chung, S. Fu, Y. Yang, An enriched multiscale mortar space for high contrast flow problems, *arXiv preprint arXiv:1609.02610* (2016).
- [16] D. Cortinovis, P. Jenny, Iterative galerkin-enriched multiscale finite-volume method, *Journal of Computational Physics* 277 (2014) 248–267.
- [17] R. T. Guiraldello, R. F. Ausas, F. S. Sousa, F. Pereira, G. C. Buscaglia, Interface spaces for the multiscale Robin coupled method in reservoir

- simulation, *Mathematics and Computers in Simulation* 164 (2019) 103–119.
- [18] A. L. Madureira, M. Sarkis, Hybrid localized spectral decomposition for multiscale problems, arXiv preprint arXiv:1706.08941 (2017).
 - [19] E. T. Chung, Y. Efendiev, W. T. Leung, An online generalized multiscale discontinuous galerkin method (GMsDGM) for flows in heterogeneous media, *Communications in Computational Physics* 21 (2) (2017) 401–422.
 - [20] E. T. Chung, S.-M. Pun, Online adaptive basis enrichment for mixed CEM-GMsFEM, arXiv preprint arXiv:1810.10730 (2018).
 - [21] J. E. Aarnes, S. Krogstad, K.-A. Lie, A hierarchical multiscale method for two-phase flow based upon mixed finite elements and nonuniform coarse grids, *Multiscale Modeling & Simulation* 5 (2) (2006) 337–363.
 - [22] O. Møyner, K.-A. Lie, A multiscale restriction-smoothed basis method for high contrast porous media represented on unstructured grids, *Journal of Computational Physics* 304 (2016) 46–71.
 - [23] Ø. S. Klemetsdal, O. Møyner, K.-A. Lie, Accelerating multiscale simulation of complex geomodels by use of dynamically adapted basis functions, *Computational Geosciences* (2019) 1–18.
 - [24] M. Peszyńska, M. F. Wheeler, I. Yotov, Mortar upscaling for multiphase flow in porous media, *Computational Geosciences* 6 (1) (2002) 73–100.
 - [25] D. Cortinovis, P. Jenny, Zonal multiscale finite-volume framework, *Journal of Computational Physics* 337 (2017) 84–97.
 - [26] M. HosseiniMehr, M. Al Kobaisi, C. Vuik, H. Hajibeygi, Dynamic multi-level multiscale simulation of naturally fractured reservoirs with generic fracture-matrix conductivity contrasts, in: *SPE Reservoir Characterisation and Simulation Conference and Exhibition*, Society of Petroleum Engineers, 2019.
 - [27] R. T. Guiraldello, R. F. Ausas, F. S. Sousa, F. Pereira, G. C. Buscaglia, The multiscale Robin coupled method for flows in porous media, *Journal of Computational Physics* 355 (2018) 1–21.

- [28] F. F. Rocha, F. S. Sousa, R. F. Ausas, G. C. Buscaglia, F. Pereira, Multiscale mixed methods for two-phase flows in high-contrast porous media, *Journal of Computational Physics* 409 (2020) 109316.
- [29] Z. Baomin, L. Jingjiang, Classification and characteristics of karst reservoirs in china and related theories, *Petroleum Exploration and Development* 36 (1) (2009) 12–29.
- [30] P. Popov, G. Qin, L. Bi, Y. Efendiev, Z. Kang, J. Li, Multiphysics and multiscale methods for modeling fluid flow through naturally fractured carbonate karst reservoirs, *SPE Reservoir Evaluation & Engineering* 12 (02) (2009) 218–231.
- [31] Z.-Q. Huang, J. Yao, Y.-Y. Wang, An efficient numerical model for immiscible two-phase flow in fractured karst reservoirs, *Communications in Computational Physics* 13 (2) (2013) 540–558.
- [32] T. V. Lopes, A. C. Rocha, M. A. Murad, E. L. Garcia, P. A. Pereira, C. L. Cazarin, A new computational model for flow in karst-carbonates containing solution-collapse breccias, *Computational Geosciences* (2019) 1–27.
- [33] V. Martin, J. Jaffré, J. E. Roberts, Modeling fractures and barriers as interfaces for flow in porous media, *SIAM Journal on Scientific Computing* 26 (5) (2005) 1667–1691.
- [34] V. Reichenberger, H. Jakobs, P. Bastian, R. Helmig, A mixed-dimensional finite volume method for two-phase flow in fractured porous media, *Advances in Water Resources* 29 (7) (2006) 1020–1036.
- [35] L. Formaggia, A. Fumagalli, A. Scotti, P. Ruffo, A reduced model for Darcy’s problem in networks of fractures, *ESAIM: Mathematical Modelling and Numerical Analysis* 48 (4) (2014) 1089–1116.
- [36] N. Schwenck, B. Flemisch, R. Helmig, B. I. Wohlmuth, Dimensionally reduced flow models in fractured porous media: crossings and boundaries, *Computational Geosciences* 19 (6) (2015) 1219–1230.
- [37] B. Berkowitz, Characterizing flow and transport in fractured geological media: A review, *Advances in Water Resources* 25 (8-12) (2002) 861–884.

- [38] B. Flemisch, I. Berre, W. Boon, A. Fumagalli, N. Schwenck, A. Scotti, I. Stefansson, A. Tatomir, Benchmarks for single-phase flow in fractured porous media, *Advances in Water Resources* 111 (2018) 239–258.
- [39] J.-G. Kim, M. D. Deo, Finite element, discrete-fracture model for multiphase flow in porous media, *AIChE Journal* 46 (6) (2000) 1120–1130.
- [40] M. Karimi-Fard, L. J. Durlofsky, K. Aziz, An efficient discrete fracture model applicable for general purpose reservoir simulators, in: *SPE Reservoir Simulation Symposium*, Society of Petroleum Engineers, 2003.
- [41] H. Hoteit, A. Firoozabadi, An efficient numerical model for incompressible two-phase flow in fractured media, *Advances in Water Resources* 31 (6) (2008) 891–905.
- [42] M. Tene, M. S. Al Kobaisi, H. Hajibeygi, Algebraic multiscale method for flow in heterogeneous porous media with embedded discrete fractures (F-AMS), *Journal of Computational Physics* 321 (2016) 819–845.
- [43] Z. Chai, B. Yan, J. Killough, Y. Wang, An efficient method for fractured shale reservoir history matching: The embedded discrete fracture multi-continuum approach, *Journal of Petroleum Science and Engineering* 160 (2018) 170–181.
- [44] E. T. Chung, Y. Efendiev, T. Leung, M. Vasilyeva, Coupling of multi-scale and multi-continuum approaches, *GEM-International Journal on Geomathematics* 8 (1) (2017) 9–41.
- [45] M. Wang, S. W. Cheung, E. T. Chung, M. Vasilyeva, Y. Wang, Generalized multiscale multicontinuum model for fractured vuggy carbonate reservoirs, *Journal of Computational and Applied Mathematics* 366 (2020) 112370.
- [46] H. Hajibeygi, D. Karvounis, P. Jenny, A hierarchical fracture model for the iterative multiscale finite volume method, *Journal of Computational Physics* 230 (24) (2011) 8729–8743.
- [47] L. Li, S. H. Lee, Efficient field-scale simulation of black oil in a naturally fractured reservoir through discrete fracture networks and homogenized media, *SPE Reservoir Evaluation & Engineering* 11 (04) (2008) 750–758.

- [48] Y. Efendiev, S. Lee, G. Li, J. Yao, N. Zhang, Hierarchical multiscale modeling for flows in fractured media using generalized multiscale finite element method, *GEM-International Journal on Geomathematics* 6 (2) (2015) 141–162.
- [49] S. Bosma, H. Hajibeygi, M. Tene, H. A. Tchelepi, Multiscale finite volume method for discrete fracture modeling on unstructured grids (MS-DFM), *Journal of Computational Physics* 351 (2017) 145–164.
- [50] Q. Zhang, Z. Huang, J. Yao, Y. Wang, Y. Li, A multiscale mixed finite element method with oversampling for modeling flow in fractured reservoirs using discrete fracture model, *Journal of Computational and Applied Mathematics* 323 (2017) 95–110.
- [51] P. Devloo, W. Teng, C.-S. Zhang, Multiscale hybrid-mixed finite element method for flow simulation in fractured porous media, *CMES-Computer Modeling in Engineering & Sciences* 119 (1) (2019) 145–163.
- [52] Y. Xia, Y. Jin, M. Chen, K. P. Chen, An enriched approach for modeling multiscale discrete-fracture/matrix interaction for unconventional-reservoir simulations, *SPE Journal* (2018).
- [53] D. W. Peaceman, *Fundamentals of numerical reservoir simulation*, Vol. 6, Elsevier, 2000.
- [54] R. E. Ewing, *The mathematics of reservoir simulation*, SIAM, 1983.
- [55] J. Douglas, F. Furtado, F. Pereira, On the numerical simulation of waterflooding of heterogeneous petroleum reservoirs, *Computational Geosciences* 1 (2) (1997) 155–190.
- [56] R. J. LeVeque, *Finite volume methods for hyperbolic problems*, Vol. 31, Cambridge University Press, 2002.
- [57] R. T. Guiraldello, R. F. Ausas, F. S. Sousa, F. Pereira, G. C. Buscaglia, Velocity postprocessing schemes for multiscale mixed methods applied to contaminant transport in subsurface flows, *Computational Geosciences* (2020) 1–21.
- [58] L. Jiang, Q. Li, Model’s sparse representation based on reduced mixed GMsFE basis methods, *Journal of Computational Physics* 338 (2017) 285–312.